

Ring Star Formation Rates in Barred and Nonbarred Galaxies

R. D. Grouchy^{1,2,3,5}, R. J. Buta^{1,2}, H. Salo³, and E. Laurikainen^{3,4}

ABSTRACT

Nonbarred ringed galaxies are relatively normal galaxies showing bright rings of star formation in spite of lacking a strong bar. This morphology is interesting because it is generally accepted that a typical galactic disk ring forms when material collects near a resonance, set up by the pattern speed of a bar or bar-like perturbation. Our goal in this paper is to examine whether the star formation properties of rings are related to the strength of a bar or, in the absence of a bar, to the non-axisymmetric gravity potential in general. For this purpose, we obtained H α emission line images and calculated the line fluxes and star formation rates (SFRs) for 16 nonbarred SA galaxies and four weakly barred SAB galaxies with rings. For comparison, we combine our new observations with a re-analysis of previously published data on five SA, seven SAB, and 15 SB galaxies with rings, three of which are duplicates from our sample. With these data, we examine what role a bar may play in the *star formation process* in rings. Compared to barred ringed galaxies, we find that the inner ring SFRs and H α + [NII] equivalent widths in nonbarred ringed galaxies show a similar range and trend with absolute blue magnitude, revised Hubble type, and other parameters. On the whole, the star formation properties of inner rings, excluding the distribution of HII regions, are independent of the ring shapes and the bar strength in our small samples. We confirm that the deprojected axis ratios of *inner rings* correlate with maximum relative gravitational force Q_g ; however, if we consider all rings, a better correlation is found when local bar forcing at the radius of the ring, Q_r , is used. Individual cases are described and other correlations are discussed. By studying the physical properties of these galaxies, we hope to gain a better understanding of their placement in the scheme of the Hubble sequence and how they formed rings without the driving force of a bar.

Subject headings: galaxies: kinematics and dynamics; galaxies: photometry; galaxies: spiral; galaxies: structure

1. Introduction

A nonbarred ringed galaxy is a normal galaxy that shows one or more large-scale ring-shaped patterns in the absence of a conspicuous bar. These galaxies are interesting because they pose a small dilemma for existing dynamical theories: based on numerical simulations, a bar is believed to be an *essential element* in ring formation (e.g., Schwarz 1981, 1984a; see also reviews by Sellwood & Wilkinson 1993; see also review

¹Visiting Astronomer, Cerro Tololo Inter-American Observatory, La Serena, Chile

²Department of Physics and Astronomy, University of Alabama, Tuscaloosa, AL, 35487-0324, USA

³Department of Physical Sciences Astronomy Division, University of Oulu, FI-90014 Oulu, Finland

⁴Finnish Centre for Astronomy with ESO (FINCA), University of Turku, Turku, Finland

⁵Now at L'Observatoire de Paris; 61 Av. de l'Observatoire, F-75014 Paris, France

by Buta & Combes 1996). These simulations have indicated that rings form easily in galaxies through bar-driven gravity torques. These torques can lead to the secular accumulation of interstellar gas into well-defined regions, usually the main low-order resonances associated with the bar pattern speed. Invariant manifolds of orbits near unstable Lagrangian points have also been proposed to explain specific characteristics of galaxy rings (Romero-Gómez et al. 2006; Athanassoula et al. 2009).

Alternate theories have been proposed to explain the presence of rings in nonbarred galaxies. One such theory suggests that nonbarred ringed galaxies were once more strongly barred, but the bar has mostly or completely dissolved, leaving behind the rings that formed when the bar was stronger. Bar dissolution might occur if a bar drives enough gas to the center to build up a central mass concentration (CMC; e.g., Shen & Sellwood 2004), or if gas exerts sufficient torques on the bar (Bournaud et al. 2005). The idea of bar dissolution and reformation is an active topic at this time (Bournaud & Combes 2002; Bournaud et al. 2005), but has not been unambiguously confirmed by observations. In 2002, Block et al. found some evidence for bar dissolution, but a similar analysis done by Buta et al. (2004) was not able to confirm the results. Buta (1991) suggested that NGC 7702 could be an example of a ringed galaxy whose main bar has dissolved because of the presence of a nuclear bar, a possible relic of a past major bar episode (Friedli & Pfenniger 1991). Athanassoula (1996) examined the effects of bar dissolution on a simulated outer ring, and found that the ring survives for a long time after the bar dissolves.

It is possible that the rings of some nonbarred galaxies formed in response to a strong spiral density wave (e.g., the SA(r)bc spiral NGC 5364). Mark (1974) suggested that a ring could form at the inner Lindblad resonance (ILR) of the spiral wave pattern speed. Buta & Combes (1996) argued that such rings would be infrequent due to the inefficiency of the ring formation process in the presence of what might be an unsteady spiral. However, Rautiainen & Salo (2000) concluded that in models with a hot disk that never formed a bar (Toomre Q -parameter=2.5), a spiral potential can still effectively form a ring at the spiral ILR.

Another possible explanation for ring formation in nonbarred galaxies is that some of these rings are in fact still bar-driven features, but the bar is only detectable in the near-infrared where the galaxy is more transparent to dust. Most galaxies are selected for given properties from catalogs that only give blue-light classifications (e.g., de Vaucouleurs et al. 1991; Sandage & Tammann 1981). Blue light is a very good passband for detecting rings, dust, and young stars, but bars tend to be made of older stellar populations that are less prominent in such a waveband. Infrared light penetrates the dust more effectively and is more sensitive to the stellar population typically found in bars. A recently identified example of a ringed galaxy classified as nonbarred in blue light but which shows a bar in the near-IR is the SA(rs)bc spiral NGC 3147 (Casasola et al. 2008). In related cases, a bar might be missed even if potentially detectable in blue light because it is viewed end-on at a high inclination angle (e.g., the Sb(r) galaxy NGC 7184; Sandage & Tammann 1981).

It is also possible that a ring of a nonbarred galaxy can form through the minor merger of a companion. Sil’chenko & Moiseev (2006) suggested that the small rings seen in NGC 7217 and NGC 7742, both known to have counter-rotating components, are due to tidally induced distortion of the stellar disk due to the (now mostly-merged) companion. Some rings, as in Hoag’s object and IC 2006, have been interpreted in terms of accretion of a gas-rich companion (e.g., Schweizer et al. 1987, 1989). These ideas have also been considered to explain the large star-forming UV ring seen in the nonbarred galaxy ESO 381–47 (Donovan et al. 2009).

In addition to the mode of ring formation, another intriguing aspect of some nonbarred ringed galaxies is the presence of counter-winding spiral patterns in which two sets of spiral structure appear to open opposite to one another. The implication, assuming both features are in the same plane and are not counter-rotating,

is that one set of spiral structure is trailing while the other is leading. The best-known example of counter-winding spiral structure is the SA(r)a galaxy NGC 4622 (Buta et al. 1992, 2003), and we have recently identified a new case in the SA(rs)bc spiral ESO 297–27 (Grouchy et al. 2008, hereafter Paper 1). In NGC 4622, the inner ring is made partly of leading and trailing arm segments, while in ESO 297–27, the inner pseudoring is made mainly of a single inner spiral arm. Although it has been suggested in these papers that such patterns could indicate that an interaction has occurred, no definitive theoretical studies have yet been made that can explain the special characteristics of each case.

In this paper, we examine the star formation properties in both barred and nonbarred ringed galaxies with several objectives in mind. First, concentrated star formation is an aspect that both barred and nonbarred galaxy rings share (Sandage 1961; Kormendy 1979; Buta 1988 and references therein; Pogge 1989; Buta et al. 2004). This would seem to point to a galaxy-wide mechanism for collecting gas into rings. We wish to examine whether any aspect of the ring-shaped star formation, such as the star formation rate (SFR), might connect to the strength of the non-axisymmetric perturbation. We are also interested in the triggering mechanism of star formation in rings. If bars actually trigger the star formation in rings, we might expect that barred galaxies will on average show higher ring SFRs. Previous studies have suggested that this is not the case. Some nonbarred or weakly barred galaxies are exceptional sites of star formation (e.g., NGC 4736 and 7742), and these make it unclear whether a bar is an essential element to the *star formation process* occurring in rings. The problem is akin to spiral structure: do density waves trigger star formation in galaxies, or do they act merely as pattern-organizing structures with little or no role in triggering the collapse of clouds? Elmegreen & Elmegreen (1986) and McCall (1986) independently concluded that density waves are not likely to be the main triggering mechanism for star formation in galaxies.

Our second objective is to re-examine how intrinsic ring shape connects to perturbation strength and ring star formation. Buta (2002) had suggested that ring shape does not depend significantly on bar strength, defined as the maximum gravitational torque per unit mass per unit square of the circular speed. This finding is at odds with numerical simulation studies (e.g., Salo et al. 1999), and we consider an alternative approach that uses the strength of the perturbation at the position of the ring as the controlling parameter for ring shape.

Our final goal is to bring more attention to the diversity of properties of the rings in nonbarred galaxies. This diversity is greater than what is seen in barred galaxy rings, whose statistical properties, such as relative sizes, shapes, and orientations relative to the bar have been studied previously (Buta 1995).

Our study is based on an analysis of new $H\alpha+[NII]$ images of 20 nonbarred ringed galaxies (Grouchy 2008) complemented by optical *BVI* images that will be more fully presented in a separate paper. In order to cover a wide range of apparent bar strengths, our sample is combined with a re-analysis of previously published data for 20 strongly barred and 12 weakly barred galaxies initially analyzed by Crocker et al. (1996, hereafter CBB96). The main finding of CBB96 was a correlation between the way HII regions are distributed around inner rings and the intrinsic axis ratio of the rings. Circular inner rings have HII regions distributed more uniformly in azimuth than do elliptical inner rings. In the latter, HII regions concentrate around the ring major axis. We also further explore this issue here.

$H\alpha+[NII]$ images are used to derive SFRs for both the global HII region distribution and for the HII regions confined to specific rings, using the flux conversion technique of Kennicutt (1983, 1998a). Previous studies (Finn et al. 2004; Kennicutt et al. 1994) have found connections between a galaxy’s type and its SFR (see Finn’s Figure 9). This paper complements these previous studies with more comparisons of the general properties of nonbarred ringed galaxies (color, absolute magnitude, equivalent width, and type) to their SFRs.

This paper is arranged as follows. In Section 2, we describe the galaxies in our sample as well as the CBB96 sample. We discuss the observations and the process of data analysis, including a re-analysis of the CBB96 data. We also describe the process of calculating the galaxy’s SFR as well as our estimates in the accuracy of the calibration. Section 3 focusses on the derivation of ring parameters and includes a description of the H α distribution for each galaxy observed. In Section 4, we explain the process of deriving the non-axisymmetric perturbations. In Section 5, we discuss the analysis of the galaxy and ring properties addressing possible correlations. The discussion of our findings and conclusions can be found in Sections 6 and 7, respectively.

2. The Data

2.1. Sample Selection

The sample of nonbarred ringed galaxies observed for this paper was selected from the Third Reference Catalogue of Bright Galaxies (RC3; de Vaucouleurs et al. 1991) and the Catalogue of Southern Ringed Galaxies (CSRG; Buta 1995). The main requirement was that the galaxy has a well-defined inner or outer ring, or both types of features. We not only chose our galaxies by morphological type, but we also constrained the isophotal galaxy diameter to $D_{25} \geq 2'$ and the isophotal axis ratio to $R_{25}^{-1} \leq 0.5$ (implying an inclination $i \leq 60^\circ$) so that we would be able to resolve the spiral and ring structures within the galaxy’s disk. The sample cannot be regarded as statistical, but merely as a set of well-defined cases. The type range is S0⁺ to Sbc, where rings are most typically found in nonbarred as well as barred galaxies.

Our data set of 20 galaxies cannot stand alone because it needs a point of comparison. We want to know how the properties of star formation in nonbarred galaxy rings might compare to what is normally seen in barred galaxies. For this purpose, the sample of CBB96 is especially useful. CBB96 observed 32 ringed galaxies and derived HII region luminosity functions, galaxy-wide SFRs, and the distribution of HII regions around inner rings, covering a wide range of apparent bar strengths, but mostly emphasizing barred galaxies.

The CBB96 sample was selected in a similar manner as our new sample, and the average properties of the two are similar. For example, the type range for the two data sets is similar, and both samples emphasize high luminosity galaxies. The latter can be seen by comparing the mean absolute blue magnitudes for the new sample ($\langle M_B \rangle = -20.4 \pm 0.8$) and the CBB96 sample ($\langle M_B \rangle = -20.4 \pm 0.6$). Combining our sample with CBB96, we have 27 nonbarred (SA and SAB) and 20 barred (SB) or weakly barred (SAB and SAB) galaxies. Since three galaxies are in common between the two data sets, the combined sample includes 44 different galaxies. Our newly observed galaxies and their general properties are listed in Table 1, while the properties of the CBB96 sample are listed in Table 2.

2.2. Observations and Reduction

Our new H α observations were obtained in 2002 August with a Tek 2K CCD camera attached to the 1.5 m telescope of Cerro-Tololo Inter-American Observatory (CTIO). The CCD was operated with a gain of 1.5 e⁻ per ADU and has a pixel scale of 0".434, giving a field of view of 14'8 x 14'8. We imaged each galaxy twice, once in the redshifted H α emission filter followed by an image offset in wavelength for continuum subtraction.

The images were reduced using standard IRAF procedures and calibrated to a standard scale by following the steps detailed in Jacoby et al. (1987). Each night, we observed spectrophotometric standard stars (Hamuy et al. 1992) in the same filters as the galaxy images. The standard stars were used to calculate the sensitivity, $S(\lambda)$, of our system, which allows us to convert the instrumental $H\alpha$ emission flux to a flux measured in $\text{erg s}^{-1} \text{cm}^{-2}$. Table 3 lists the calculated sensitivity of our system for each star observed. Using a 3σ rejection, we adopted a mean value of $S(\lambda)$ for each filter. We observed the spectrophotometric standard stars through all filters available; however, seven observations were omitted either due to tracking problems or the fact that the filter was not used that night.

To measure the amount of $H\alpha$ emission from each galaxy, we first subtracted the continuum from the redshifted $H\alpha$ image. Each filter is approximately 75 \AA wide and has a unique transmission profile, which depends on wavelength (see Figure 1). Due to this variation in transmission properties for each filter, the nearby continuum may not be an accurate model of the continuum underlying the $H\alpha$ emission. Since stars are not strong sources of $H\alpha$ emission, their fluxes are expected to be the same in both images, and any difference in the foreground stellar flux measurements is attributed to differences in filter properties. After matching the point-spread function of the foreground stars, we modified the nearby continuum to approximate the underlying continuum in the $H\alpha$ image by using the ratio of the flux from these stars as a scale factor. In many cases, we find a residual flux after subtracting the scaled continuum. Using these residuals, we find a range of 0.1%-9.1% uncertainty in the continuum subtraction from the $H\alpha$ image (see Table 4). We must keep these uncertainties in mind for galaxies in our samples with low levels of emission which may be artifacts from this subtraction process.

After subtracting the continuum, the sky, and the residual foreground star fluxes from the line images, the total $H\alpha$ fluxes were integrated within ellipses having the shape and orientation listed in Table 1. The sizes of these ellipses were determined by the visible extent of the observed $H\alpha$ emission.

According to a survey done by Kennicutt & Kent (1983) on ≈ 170 galaxies, the average equivalent width of $H\alpha$ emission from a typical galaxy ranges from 20 to 30 \AA . The narrowband filters we used are wide enough so that the additional emission lines, [NII] $\lambda 6548$ and $\lambda 6584$, contribute to the measured $H\alpha$ flux. This contamination is removed from each measurement by using an estimated average ratio of [NII] to $H\alpha$ of 0.5 for normal spiral galaxies (Kennicutt et al. 1994). Table 4 summarizes the $H\alpha + [\text{NII}]$ fluxes for our sample and the CBB96 sample. We then converted these fluxes ($\text{erg s}^{-1} \text{cm}^{-2}$) to a luminosity (erg s^{-1}) by using NASA/IPAC Extragalactic Database (NED) Galactic standard of rest (GSR) distances to the galaxies (see Table 1). NED distances assume a cosmological expansion rate of $H_0 = 73 \pm 5 \text{ km s}^{-1} \text{Mpc}^{-1}$.

2.3. Calculation of Star Formation Rate

We corrected our $H\alpha$ luminosity for extinction within the galaxy (internal extinction) as well as absorption of $H\alpha$ emission between the galaxy and our detector (Galactic extinction). Kennicutt et al. (1994) found, on average, that the internal extinction in a typical HII region of a normal spiral galaxy is approximately 1.1 mag. The Galactic extinction, on the other hand, was calculated for each galaxy in Table 1 using Seaton’s (1979) relation of

$$A(\lambda) = E(B - V) \times X(\lambda), \quad (1)$$

where $E(B - V)$ is the Galactic extinction taken from NED and $X(6563)$, the interstellar extinction at 6563 \AA , is taken to be 2.46 (Howarth 1983). Both sources of extinction were subtracted from the $H\alpha$ magnitude to get the corrected luminosities listed in Column 6 of Table 4.

The H α luminosity was used as a direct measure of the SFR within a galaxy. Kennicutt, Tamblyn, & Congdon (1994) tested the rate of star formation for galaxies with varying initial mass functions. They found the relation of $1M_{\odot} \text{ yr}^{-1} = 1.26 \times 10^{41} \text{ erg s}^{-1}$ based on a Salpeter (1955) initial mass function with a mass range from $0.1 M_{\odot}$ to $100 M_{\odot}$. This relation assumes solar metallicity and a constant SFR for the galaxy. Our SFRs for the 20 galaxies are listed in Table 4.

We estimated the equivalent width of H α emission for each galaxy by comparing the H α flux to that of the scaled continuum image. This is a distance-independent parameter (owing to normalization by the continuum flux) that has been interpreted as a ratio of current to past star formation (e.g., Hameed & Devereux 1999). We used the following relationship to calculate the equivalent width (Romanishin 1990):

$$W_{\lambda} = \int \frac{(F_{obs} - \alpha F_{cont})}{\alpha F_{cont}} \times \frac{T_{\lambda}}{T_{H\alpha}} d\lambda, \quad (2)$$

where F_{obs} is the flux from the H α image, F_{cont} is the flux from the continuum image, α is the scale factor determined from foreground stars, $T_{H\alpha}$ is the transmission coefficient of the filter at the galaxy’s redshifted H α emission, and T_{λ} is the fraction of light with wavelength λ , which is transmitted through the filter. All values calculated from the narrowband images such as $L_{H\alpha}$, SFR, and W_{λ} are listed in Table 4.

For the CBB96 sample, the observations, image processing techniques, and calibration are fully described in CBB96 and will not be repeated here. The original analysis of these data is in any case similar to what we have done in this paper with the exception that we have used the York Extinction Solver (McCall 2004) to correct the fluxes for Galactic extinction.

2.4. Accuracy of Calibrations and Flux Measurements

To test the accuracy of the calibration of the new sample, we observed the planetary nebulae NGC 6818 and NGC 6326 through the H α and the nearby continuum filters. We applied the system’s sensitivity to the planetary nebulae using the following equation from Jacoby et al. (1987):

$$S(\lambda) = \frac{F(\lambda)}{C \times 10^{0.4K(\lambda)A}}, \quad (3)$$

where $F(\lambda)$ is the known flux of the planetary nebulae at wavelength λ , C is the photon count rate, $K(\lambda)$ is the CTIO atmospheric extinction, and A is the airmass. These nebulae were the subject of a previous study by Kohoutek & Martin (1981, hereafter KM81); therefore, the H α fluxes ($F(\lambda)$ in Equation (3)) for these nebulae are known. We used the IRAF routine PHOT to measure a count rate within an aperture large enough to enclose the optical extent of the nebula. By comparing our measured fluxes to those of KM81, we found that, on average, our calibration was too bright by ≈ 0.15 mag. This discrepancy may indicate that our aperture sizes were larger than those used by KM81; however, we were unable to confirm this as the source of the error since the aperture sizes were not listed in KM81. Our observations compared with measurements from KM81 are listed in Table 5. The KM81 values refer to the sum of the H α and [NII] fluxes listed in their paper.

For our purposes, we need more information from the CBB96 sample than was given by CBB96. First, we wanted to estimate ring SFRs for the CBB96 galaxies in a similar manner as we have derived them for our present sample. Second, we wanted to derive quantitative estimates of bar strength for this sample to more firmly examine the possible significance of bars in the ring star formation process. These parameters

necessitated that we re-analyze the original CBB96 images. The main difference with CBB96 will be in the selection of foreground stars for the continuum subtraction and minor details of the sky subtraction. Therefore, we can evaluate the *internal* uncertainties in the continuum subtraction simply by the action of two independent analyses of the same data set. Figure 2 shows a comparison between the revised total $H\alpha$ fluxes (see Table 6) for the CBB96 sample and those listed in Column 2 of Table 7 of CBB96. The line is a perfect correlation for comparison. The re-analysis differs from the original analysis in the sense $\langle \log(CBB96_{original}/CBB96_{revised}) \rangle = 0.08 \pm 0.03$ with a standard deviation of 0.15 dex for 26 objects. The scatter of ± 0.15 dex is larger than the 20% uncertainties Kennicutt (1983) quoted as typical in $H\alpha$ flux measurements, but this is not surprising given the early Hubble types and the faintness of the emission in many cases. Table 6 summarizes the results of our re-analysis of the CBB96 data.

Our sample shares three galaxies with CBB96, and it shares three galaxies with a study done by Kennicutt & Kent (1983, hereafter KK83). Figure 3 compares the $H\alpha + [NII]$ fluxes of our galaxies with the measurements from CBB96 and KK83. The mean difference between the log of our flux and that from CBB96 or KK83 (i.e. $\langle \log(F/F_{other}) \rangle$) for all six galaxies is -0.14 with a standard error in the mean of ± 0.14 . The standard deviation of each flux estimate is 0.33 which is about twice as high as the standard deviation of the internal comparison in Figure 2. The scatter is larger than for the typical late-type galaxies studied by KK83 owing partly to the relatively early types of the galaxies and to the faintness of the emission. Similarly, the CBB96 sample shares galaxies with previous studies. Figure 4 compares the revised measurements from the CBB96 sample with the measurements from one galaxy in the KK83 sample, two galaxies studied by Hameed & Devereux (1999), and two galaxies studied by Koopmann & Kenney (2006). The agreement is very good for four of the galaxies. The discrepant point is NGC 1350, which suffers from serious scattered light on the CBB96 image.

3. Derivation of Ring Parameters

3.1. $H\alpha$ and Star Formation in the Rings

In addition to *global* $H\alpha$ fluxes and SFRs, we measured these values for the rings in the sample. For this purpose, we fitted an ellipse to the projected $H\alpha$ ring to determine its size and ellipticity. Using IRAF routine TVMARK, we visually selected prominent HII regions and regions of diffused emission assumed to be associated with the ring feature. This method isolated the ring along the line of its maximum $H\alpha$ emission. Next, a least-squares fit was used to derive the center coordinates, major and minor axes dimensions, and major axis position angle (P.A.). If a ring was not visible in the $H\alpha$ image, then its parameters were determined from the broadband image. We acknowledge the potential for variations in the ring parameters based on the shape defined by the observer. To estimate this error, two individuals measured the ring properties independently. The size of the semimajor axis radius was affected less than the ring’s axis ratio with errors that were, on average, 0.6% and 1.8% of the fitted values, respectively. To approximate a total error in our ring sizes and shapes, we added, in quadrature, the human error with the error resulting from fitting the points to an ellipse. We calculated the parameters for inner and outer rings as noted in the galaxy’s Hubble–de Vaucouleurs type. Here we establish the convention of defining the “main” ring of the galaxy as the inner ring unless the galaxy has no inner ring (e.g., NGC 7020, 7217, and IC 1993) in which case the main ring refers to the outer ring. We then used the IRAF routine ELLIPSE to measure the flux within an elliptical annulus encompassing the projected ring. We found that the shape and P.A. of the rings rarely coincided with the same values derived from the outer isophotes of the broadband images (Grouchy

2008). Table 7 lists the diameter, width, shape, P.A., and SFR of the projected rings while Table 8 shows the deprojected size and shape of the main ring.

For the CBB96 data, a similar procedure was followed to define the ring properties. We used a cursor on a TV display to map out the size, shape, and major axis P.A. of the inner rings, and then fitted these points with an ellipse. Then an elliptical annulus encompassing the entire inner ring was defined by visual inspection and the $H\alpha$ flux within that annulus was recorded. These newly derived $H\alpha$ luminosities and SFRs will differ somewhat from CBB96 who used slightly different distances. Also, we used the York Extinction Solver (McCall 2004) to correct the revised CBB96 fluxes for the small amounts of Galactic extinction in these cases. Table 6 includes our new estimates of the ring to total flux ratios of the CBB96 sample, together with the ellipse parameters used. These ratios range from essentially zero in NGC 7702 to 91% for the barred galaxy NGC 53.

3.2. Description of $H\alpha$ Distributions

Grouchy (2008) showed that most rings in the Table 1 sample are zones of enhanced blue colors, indicating active star formation. Thus, we expect that some rings will also be zones of ionized gas enhancement. In this section, we show the $H\alpha$ images and describe the characteristics of the distribution of HII regions.

The images are presented in Figures 5 - 11 with each row showing data for a single galaxy. The first column is a log scale B -band image with the galaxy name labeled in the lower left corner. The middle column is an $H\alpha$ emission image with the galaxy type in the lower left corner. The B -band and $H\alpha$ images for a single galaxy are shown in the same scale which is listed in the figure description. The third column compares the galaxy’s B -band (Grouchy 2008) and $H\alpha$ surface brightness profiles, which are azimuthally averaged radial profiles. The profiles were measured in the plane of the galaxy with elliptical orientation parameters based on the broadband images as listed in Grouchy (2008). In order to compare the two profiles, the $H\alpha$ surface brightness was assigned an arbitrary zero point of 18.945 mag just as Koopmann & Kenney (2006) did in their $H\alpha$ survey.

ESO 111–22 (Figure 5, top row). A strong example of a double-ringed nonbarred galaxy, type (R)SA(r)b, with a prominent, smooth inner ring and a large, patchy outer ring seen in the B -band. In spite of the obvious B -band morphological differences, the two rings of ESO 111–22 both show discrete HII regions, the inner ring being especially prominent. Near-side extinction may be causing the inner ring to be weak on the east side. The rings appear asymmetric; the outer ring, in particular, appears distorted from a smooth oval shape.

Of particular interest are the sizes of the two rings in this galaxy. Using measured dimensions in arcseconds and the GSR distance scale of $0.645 \text{ kpc arcsec}^{-1}$, we derive diameters of 20.1 and 63.1 kpc for the inner and outer rings, respectively. The ring diameters are much larger than the typical rings in nonbarred galaxies studied by de Vaucouleurs & Buta (1980). This is discussed further in Section 5.2. The ratio of projected ring diameters is 3.1 (see Table 8), larger than is typically seen in double-ringed barred galaxies (see review Buta & Combes 1996). We estimate that the main ring of ESO 111–22, the inner ring, contributes 26% of the galaxy’s total $H\alpha$ emission while the outer ring contributes 13%.

Comparing the surface brightness profiles for ESO 111–22 shows what appears to be an offset in the positions of the azimuthally averaged peak of emission for the inner ring from the B -band to the $H\alpha$. The B -band ring peaks around $12.''5$ while the $H\alpha$ ring peaks around $20''$.

ESO 198–13 (Figure 5, middle row). This galaxy is classified as type (R)SA(r)ab. ESO 198–13 actually has three ring features, but only the inner two are displayed in the image. The small, bright ring close to the nucleus was interpreted by Buta & Crocker (1993) and Buta (1995) as a *nuclear* ring since it is very much the analog of a nuclear ring in a barred galaxy. However, this feature has a linear diameter of 4.76 kpc, considerably larger than the average nuclear ring diameter of 1.5 kpc ($H_o = 75 \text{ km s}^{-1} \text{ kpc}^{-1}$; Buta & Crocker 1993). For the purpose of clarity, we will continue to refer to this feature as a nuclear ring even though it may be analogous to an inner ring.

In $H\alpha$, the nuclear ring is a prominent well-defined feature with discrete HII regions and some central emission. This ring appears normal and symmetric around the center of the galaxy. The larger, more flocculent pseudoring appears in the B -band image as a single spiral arm wound $\approx 520^\circ$, but it also could be a superposition of two rings offset from each other. This region appears in the $H\alpha$ image as scattered discrete HII regions. The outer ring refers to a larger, faint ring not displayed in the image because the ring did not have any $H\alpha$ emission to show.

The nuclear ring, inner pseudoring, and outer ring have measured diameters of 4.76kpc, 16.8kpc, and 49.9kpc with the outer ring measurement taken from the B -band image since the ring does not have any ionized gas. The ratio of the outer to inner pseudoring diameter is 3. However, if the nuclear ring is interpreted as an inner ring instead, then the ratio increases to 10.5. The ratio of the pseudoring to the nuclear ring diameters is 3.5, which is still larger than the mean barred galaxy outer to inner ring ratio of only 2.2 (Buta 1995). We have calculated that the nuclear ring emits 12% of the total $H\alpha$ while the main inner pseudoring contributes 55% of the emission.

From the surface brightness profiles for ESO 198–13, we see that the location and width of the stellar and gaseous rings are similar. The galaxy appears not to have diffuse ionized gas outside these ring features which is indicated by the sharp dropoff in $H\alpha$ surface brightness outside the rings. Therefore, we can say that the ionized gas is confined to the inner and nuclear rings, and it follows the spiral pattern.

ESO 231–1 (Figure 5, bottom row). This galaxy is classified as an (R')SA(r)b. There are two rings, an inner ring and an outer pseudoring. Both features are strongly represented in the narrowband $H\alpha$ image. The inner ring appears to be doubled or has a double spiral feature tightly wound into the appearance of a ring. The $H\alpha$ emission is strong, well ordered, and follows the stellar spiral structure seen in the B -band image.

The ring sizes are not as extreme in this case as the previous cases. The inner ring has a diameter of 12.2 kpc, still large for an SA galaxy according to de Vaucouleurs & Buta (1980) and emits 43% of the galaxy's $H\alpha$ emission. The outer pseudoring is 29.5 kpc in diameter, 2.4 times larger, and emits only 18% of the $H\alpha$.

The surface brightness profiles appear normal and follow each other fairly well with the two rings seen in both profiles. The placement and width of the rings are in agreement.

ESO 234–11 (Figure 6, top row). This galaxy is classified as an (R)SA(r)0⁺. Since ESO 234–11 is an early-type galaxy and does not have a lot of gas present, we would not expect to see strong $H\alpha$ emission from it. While the B -band image shows a faint hexagonal outer ring, the narrowband image shows very little ionized gas mainly from the center of the galaxy. The rings are not visible in the $H\alpha$ image, implying that they are made up of an older stellar population. The lack of ionized gas in the rings is also reflected in the $H\alpha$ surface brightness profile. The ring diameters based on the B -band image were measured to be 8.0 kpc and 23.5 kpc giving a ratio of 2.9.

ESO 236–29 (Figure 6, middle row). ESO 236–29 appears to be a relatively normal (R)SA(r)a galaxy with three ring features. Two of the three ring features are partly seen in the H α image: the nuclear and the inner rings. The inner ring appears mostly complete and consists of discrete HII regions. The strongest feature in H α is from the center of the galaxy where ionized gas follows a more elongated distribution than the apparent stellar bulge isophotes. The similarity between the shape of the inner ionized gas distribution and the outer disk suggests that ESO 236–29 has an inner ionized gas disk. In blue light, the inner ring is a well-defined feature possibly made of tightly wrapped spiral structure. The outer ring could also be interpreted as being made of a single spiral arm.

Interestingly, the high radial velocity of ESO 236–29 places it at a distance of 218.6 Mpc, leading to enormous sizes for all of its apparent ring features: 12.1 kpc for the nuclear ring, 40.9 kpc for the inner ring, and 73.8 kpc for the outer ring. The galaxy has been interpreted as a collisional ring galaxy by Madore et al. (2009), which could in principle explain these large sizes. The ratio of outer to inner ring is only 1.8 while the ratio of inner to nuclear ring is 3.4. The nuclear ring contributes 18% of the H α emission, while the main inner ring contributes only half as much with 9% of the galaxy’s H α .

The *B*-band and H α profiles appear similar to each other except for a more pronounced H α peak occurring around 7". The analogous feature in the *B*-band profile appears flatter and may be a lens-like feature instead of as a true ring.

ESO 286–10 (Figure 6, bottom row). This galaxy is classified as an (R')SA(r)a. In the *B*-band image, we see a single, faint, off-center ring which is the outer pseudoring. It appears to be made mostly of a single spiral arm, although a second outer arm is definitely present on the east side. There is very little H α emission in the ring-arm or in the galaxy as a whole. The nucleus has some ionized gas, but we only see small patches of very faint emission from the outer ring of the galaxy. The inner ring is a partial feature only weakly evident in *B* and completely invisible in H α .

We estimate the size of the outer ring to be 43 kpc and find that it contributes approximately 10% of the galaxy’s total H α emission.

Both the *B*-band and H α profiles are featureless. The H α profile shows no emission in the inner 30" after a drop off from the nucleus. Even though the outer ring is not visible in the H α image, its presence can be discerned by an increase in the H α profile beginning around 45".

ESO 297–27 (Figure 7, top row). This galaxy is classified as an SA(rs)bc and was studied in greater detail in Paper 1. It appears, at first glance, to be a normal intermediate to late-type spiral galaxy. However, a closer inspection of the *B*-band images shows a single inner arm winding counter to faint outer arms. There is no trace of the counter-winding structure in the H α emission of the galaxy which appears patchy and disorganized.

Using the *B*-band image, the inner pseudoring is approximately 15.0 kpc in diameter and a corresponding ring in the H α image is responsible for 7% of the emission.

The H α surface brightness profile follows the broadband profile fairly well including a sharp dropoff beginning around 45". The H α image as well as the surface brightness profile implies that there is a disk of diffuse ionized gas present throughout the galaxy, but it is not organized into a ring.

ESO 399–25 (Figure 7, middle row). This galaxy is classified as an (R')SA(s)0/a. The *B*-band image shows a faint outer ring, which is not seen in the H α image. As an early-type galaxy, there is little or no ionized gas seen in the narrowband image.

Using the broadband ring derived parameters, we estimate the outer ring to be 32 kpc in diameter; however, since it has no measurable ionized gas, it is an older stellar component. The lack of dust and ionized gas is reflected in the featureless profiles of the broadband and narrowband images. The $H\alpha$ profile shows a sharp drop off of emission beyond the center into what appears to be a very faint ionized disk. The majority of $H\alpha$ emission detected from this galaxy comes from the center.

ESO 409–3 (Figure 7, bottom row). This galaxy is classified as an (R')SA(s)ab. The galaxy has a faint pseudoring of $H\alpha$ emission, which follows the pseudoring seen in the B -band image. Most of the ionized gas is concentrated near the center of the galaxy. We estimate that the pseudoring has a diameter of 36.5 kpc and emits 53% of the galaxy's $H\alpha$.

The $H\alpha$ surface brightness profile of this galaxy shows a drop in emission from the center to the ring. The ring is seen in the $H\alpha$ profile and image, but it is not as broad as the stellar component.

ESO 526–7 (Figure 8, top row). This galaxy is classified as an SA(r)b. In the B -band image, we note the presence of a broad inner ring with patchy, multi-armed spiral structure continuing beyond the ring. This inner ring is also seen as a patchy narrow ring of emission in the $H\alpha$ image. The inner ring has a diameter of 21.6 kpc and emits 15% of the total $H\alpha$ flux from the galaxy. The $H\alpha$ and the B -band profiles are similar to the ionized gas tracing the inner ring as well as the spiral structure beyond.

ESO 576–57 (Figure 8, middle row). This galaxy is classified as an (R)SA(r)ab. Two rings are seen in the B -band image: a thin outer ring and a more diffuse inner ring. Neither feature is exceptionally strong, and the outer ring is only partially present. The $H\alpha$ emission does not reflect this structure however. A small amount of ionized gas was detected in the center of this early-type galaxy, and the stellar rings show very little sign of $H\alpha$ emission. While the low level of $H\alpha$ emission throughout the galaxy may be real, it may also indicate that our observations were made through the incorrect filter. At the time of the observations, the recessional velocity was listed on NED as $8883 \pm 53 \text{ km s}^{-1}$. However, it is now listed at a much lower value of $4627 \pm 10 \text{ km s}^{-1}$.

In linear dimensions, the inner and outer rings are 13.2 and 20.6 kpc in diameter, respectively. Therefore, the ratio of outer to inner ring diameter is 1.6. The main inner ring was estimated to contribute 11% of what little $H\alpha$ was detected from the galaxy.

The B -band and $H\alpha$ surface brightness profiles appear smooth and follow each other closely in shape. Even though the image does not show much $H\alpha$ emission, the disk of ESO 576–57 does appear to be filled with diffuse ionized gas.

IC 1993 (Figure 8, bottom row). This galaxy is a low-luminosity member of the Fornax Cluster and is classified as an (R')SA(s)b. The broadband image is taken from Buta & Crocker (1991) and shows the flocculent but distinctive outer pseudoring, which appears as multiple spiral arms winding into each other. The outer pseudoring appears in the $H\alpha$ image mainly as discrete HII regions, although many also lie inside the feature. The brightest of the HII regions is on the western side of the galaxy, which corresponds to the side with relatively stronger and less flocculent spiral structure in the B -band. There appears to be no real presence of ionized gas in the center of the galaxy. We find that the outer pseudoring has a diameter of 5.7 kpc and emits 80% of the galaxy's $H\alpha$.

The profile of $H\alpha$ emission for IC 1993 shows that no ionized gas was detected in the center of the galaxy. The profile does show a few patchy peaks of emission corresponding to the flocculent pseudoring seen in the broadband image.

IC 5267 (Figure 9, top row). This galaxy is classified as an (R)SA(rs)0/a. The broadband image shows two thin rings of spiral structure, which are intermittently traced by HII regions in the narrowband image. Overall, the galaxy has very little H α emission; however, the emission it does have appears to follow the spiral arms. The *B*-band image shows a minor axis dust lane, suggesting that IC 5267 has suffered a recent minor merger that may account for its complex structure.

We find that the inner and outer ring features have diameters of 18 kpc and 33 kpc, and output 4% and 6% of the galaxy’s H α flux, respectively. The ratio of outer to inner ring diameter is 1.8.

The H α emission profile shows areas of emission corresponding to the inner pseudoring and the outer ring of the galaxy. The profile drops rapidly from the center, but emission increases at around 30". A similar profile is seen in the *B*-band image, but the change in the profile corresponding to the rings is more gradual in this filter. The features may be more difficult to discern in the broadband image due to the disk being dominated by light from the bulge (see Grouchy 2008 for bulge-disk properties of this galaxy).

NGC 5364 (Figure 9, middle row). This galaxy is classified as an SA(r)bc. It is an intermediate to late-type galaxy with bright grand design spiral structure. An off-center inner ring prominently stands out against the underlying disk and the surrounding spiral arms in the *B*-band image. The arms are traced strongly by HII regions of ionized gas. The ring itself appears to have more H α emission on the northern side of the galaxy when compared to the southern side. This trend appears true for all of the spiral structure; there is a northwestern side dominance in the presence of ionized gas. NGC 5364 has a major companion, NGC 5363, to the north that may be influencing its apparent morphology. The inner ring diameter is measured to be 6.7 kpc and emits 15% of total H α flux.

The H α emission profile of NGC 5364 is patchy, showing many peaks of emission corresponding to the spiral structure. The center of the galaxy shows no emission, and the inner ring appears to be the point of first H α detection. The emission from the inner ring peaks around 30" and is much narrower than the corresponding feature seen in the broadband profile. In general, the *B*-band profile shows similar features as the H α profile, but each feature appears narrower in the narrowband.

NGC 5530 (Figure 9, bottom row). This galaxy is classified as an SA(rs)c. The spiral structure is patchy and disorganized in both the *B*-band and H α images. We do get the sense of an inner pseudoring in the *B*-band, which is not seen outlined by the HII regions. These HII regions, instead, appear unorganized and randomly distributed. The inner pseudoring is 4.6 kpc in diameter and emits 14% of the galaxy’s total H α flux.

The broadband surface brightness profile shows an increase in flux around 35" followed by an increase in H α flux around 40". This increased emission is likely due to HII regions associated with the inner pseudoring. There is a second feature of increased emission occurring approximately at 80", which is likely due to the flocculent spiral structure outside the ring. Also interesting to note is that the optical disk extends well beyond any significant H α emission.

NGC 7020 (Figure 10, top row). This galaxy is classified as type (R)SAB(r?)0/a. Although exceedingly regular and well-defined, the interpretation of its bright inner hexagonal zone as an inner ring and/or a bar is uncertain (Buta 1990b; Buta et al. 2007).

The *B*-band image shows that the large outer ring is completely detached from the inner hexagonal zone of the galaxy. The possible inner ring shows ansae at the ends of its major axis. This is a very striking galaxy for ring structure, which is not reflected in the H α emission. Although the center is bright in H α , the inner hexagonal zone and the two bright ansae are not visible in H α , confirming their stellar dynamical

nature. The galaxy appears to be fairly free of ionized gas, which is not surprising for an early-type galaxy. The outer ring has a measured diameter of 33.6 kpc and is responsible for 31% of the galaxy’s H α emission.

The surface brightness profiles of NGC 7020 appear smooth and show emission from the outer ring in H α and in the B -band. Within the outer ring, the H α profile does not show much emission except at the very center. While the H α image does not show the ansae features, the profile does indicate a slight increase in flux at their location of approximately 35'' radius.

NGC 7187 (Figure 10, middle row). This galaxy is classified as (R)SAB(r)0⁺. The morphology consists of a very faint outer ring and a striking inner ring, which appears normal and symmetric. There appears to be no strong bar, but the bulge shows isophote twists, and there may be up to three bar-like features (Buta 1990a; Wozniak et al. 1995). While the B -band image shows both rings, only the inner ring appears in the H α emission. Even though this is an early-type galaxy, gas ionized from a possible recent event of star formation exists in the inner ring feature. Perhaps this is a relatively young, new feature of the galaxy while the outer ring is an older stellar component. The inner ring has a diameter of 7.0 kpc and emits 54% of the galaxy’s total H α flux.

The B -profile shows the underlying light due to the large bulge of this early-type galaxy, which broadens the detectable ring features. The H α emission from the inner ring is seen well in the narrowband surface brightness profile as well as the image. This ring does coincide with a stellar feature, but the narrowband emission is much narrower. The H α profile also shows a slight increase in the emission from 35'' to 60'' which follows a similar stellar feature and coincides with the position of the outer ring at 51.''5.

NGC 7217 (Figure 10, bottom row). This galaxy is classified as type (R)SA(r)ab. It has a large, flocculent outer ring with a sharp, well-defined inner ring inside the bright bulge. The outer ring appears to be the main source of H α flux from this galaxy. There is a wide zone of HII regions surrounding the inner ring, and this zone has a sharp, ring-like boundary on its outer edge. Thus, NGC 7217 appears to be an example of a three-ring nonbarred galaxy. The illustrated broadband image is from Buta et al. (1995).

The inner ring has a diameter of 1.7 kpc and contributes 4% of the total H α emission. This ring has a zone of HII regions surrounding it which extends out to a diameter of 5.1 kpc. The outer ring is approximately 12.0 kpc in diameter and 1.4 kpc wide.

The B -band profile is smooth and shows the broadened stellar outer ring feature. On the other hand, the H α profile shows little emission, and the emission is sporadic. Of the emission that was detected, the majority of it comes from the outer ring.

NGC 7702 (Figure 11, top row). This galaxy is classified as an (R)SAB(r)0⁺. It has a faint outer ring, not displayed in the B -band image, which was not visible in the H α image. NGC 7702 also has an inner ring which is very striking in the broadband image, but mostly disappears in the narrowband image.

The inner ring of NGC 7702 has a diameter of 13.7 kpc and emits 22% of the total H α flux coming from this galaxy. These measurements are based on the inner ring orientation parameters derived from the B -band image.

While the H α image does not show any significant emission, the surface brightness profile does show an increase in flux around 30'' which coincides with the inner ring in the broadband. Although we were unable to detect any significant H α emission from the outer ring, there does seem to be an increase in H α flux beginning around 70'' which corresponds to the approximate location of the outer ring as seen in the broadband.

NGC 7742 (Figure 10, bottom row). This galaxy is classified as type $SAB(r)ab$, where the weak bar classification recognizes a small, broad oval located inside the inner ring. It has an inner ring that shows up strongly in the broadband and the narrowband images. The ionized gas appears to be distributed in a disk outside of this ring. The ring itself, in the narrowband image, when viewed closely, takes on the shape of two extremely well-defined and tightly wound spiral arms (see Figure 12). de Zeeuw et al. (2002) showed that the gas in NGC 7742 is rotating counter to the stellar background disk. Thus, the extreme appearance of this galaxy may be due to a merger of two galaxies. The inner ring has a diameter of 2.26 kpc and emits 87% of the galaxy’s $H\alpha$ flux.

The intense $H\alpha$ emission from the inner ring appears as a narrow, sharp peak in the surface brightness profile. The B -band profile shows that the ring coincides with the $H\alpha$ ring, but the stellar ring feature is not as dramatic.

3.3. Ring Diameters

Comparing absolute blue magnitudes from Grouchy (2008) for the galaxies in Table 1 to the magnitudes from CBB96 for the Table 2 sample, we find the same mean, $\langle M_B^o \rangle = -20.4 \pm 0.7$, suggesting it is reasonable to compare the two samples. Nevertheless, we have noted in Section 3.2 the large diameters of some of the rings in the Table 1 sample. This suggests a selection bias toward larger than average rings. To get an idea of how much larger the rings might be, we use the analyses of de Vaucouleurs & Buta (1980) and Buta & de Vaucouleurs (1982). De Vaucouleurs & Buta analyzed ratios of ring diameters to galaxy diameters for a sample of nearby galaxies, and they found that relative ring sizes depend on family (i.e., barred or nonbarred) and stage (i.e., early, intermediate, or late type). They found that nonbarred galaxy rings have a smaller relative size than barred galaxy rings and that early- and late-type galaxies have rings smaller in relative size than intermediate types.

Buta & de Vaucouleurs (1982) then used a subset of galaxies having known distances from various methods to calibrate the linear diameters of the rings. Again, these diameters were found to depend on family and stage. After an adjustment for the distance scale used by Buta & de Vaucouleurs (1982), which was consistent with a Hubble constant of $100 \pm 10 \text{ km s}^{-1} \text{ Mpc}^{-1}$ (de Vaucouleurs & Bollinger 1979), Figure 13 shows the stage and family dependence for linear ring diameters. The upper dashed lines are for $SB(r)$ and $SB(rs)$ galaxies, while the lower dashed lines are for $SA(r)$ and $SA(rs)$ galaxies. SAB galaxies would be intermediate between these lines. The points plotted on this graph are for our combined barred/nonbarred galaxy sample, with filled circles for SB types, crosses for SAB types, and open circles for SA types. The diameters are from Tables 8 and 9. The plot shows that indeed our rings are larger than the typical features seen in nearby galaxies, for both barred and nonbarred but especially for the nonbarred galaxies. In fact, the largest and smallest inner rings are found among the SA galaxies. The larger scatter in SA ring diameters compared to SB ring diameters was also found by de Vaucouleurs & Buta (1980) and Buta & de Vaucouleurs (1982).

In a substantial revisiting of the general ring size issue, Wu (2008, 2009) has completely reconsidered the dependence of ring radii on galaxy parameters using a sample from the CSRG which is statistically more complete. Wu found little evidence for the stage and family dependences highlighted by Buta & de Vaucouleurs, at least for galaxies earlier than Sc . Wu develops a relation between absolute near-infrared magnitudes, corrected to have a Gaussian error distribution, and the log of the linear ring diameter D in kiloparsecs, and finds that the near-IR luminosity $L_{IR} \propto D^{1.2}$, significantly different from the D^2 relation

found by Kormendy (1979) for blue-light absolute magnitudes. Wu argues that the Buta & de Vaucouleurs and Kormendy samples suffered biases or selection effects, and indeed for nonbarred galaxies the issue of ring distinctions (i.e., nuclear versus inner) can contribute to an apparent family dependence in ring sizes. Figure 13 shows that the barred and nonbarred galaxies in our combined samples have similar average diameters, likely because the CSRG would not have detected the nuclear ring analogs in SA galaxies.

4. Derivation of Non-Axisymmetric Perturbations

The gravitational torque method (Combes & Sanders 1981; Buta & Block 2001; Laurikainen & Salo 2002) was used to derive quantitative estimates of the maximum non-axisymmetric perturbation in the combined barred/nonbarred ringed galaxy sample. The method, described in Laurikainen & Salo (2002), is based on transforming a red or near-infrared image into a gravitational potential under the assumption of a constant mass-to-light ratio. We use a polar method to convert two-dimensional images into two-dimensional potential maps (see Salo et al. 1999 for details). The polar method reduces the noise which is helpful in the fainter, outer regions of the galaxy. The potential is written as the convolution of the density with the function $1/\Delta r$, modified to allow for finite disk thickness. From these potentials, the radial, F_R , and tangential, F_T , force components are derived. Also, from the $m=0$ Fourier component of the potential, the mean radial force, F_{0R} , is derived. For barred galaxies, a measure of the bar strength is derived from the ratio map F_T/F_{0R} . In the presence of a bar, this kind of map shows a “butterfly” pattern with islands of strong relative tangential forcing (see Figure 14). The sign of the tangential force is dependent on a quadrant because this force component always points toward the bar ends. From the ratio map, we interpolate the following function:

$$Q_T(r) = \frac{|F_T(r, \phi)|_{max}}{|F_{0R}(r)|}. \quad (4)$$

The maximum of this function, Q_g , gives a single measure of the total non-axisymmetry strength (see Figure 15). If the galaxy has a significant bar, Q_g is the same as the bar strength, Q_b , while if a galaxy has a strong spiral but a weak or no bar, then Q_g is a measure of the spiral strength, Q_s . For a galaxy with an elongated ring, the maximum value of Q_T , at the *deprojected major axis radius of the ring*, is a measure of the non-axisymmetric force felt by the ring, which we will call Q_r (see Figure 15).

For the 20 galaxies in our present sample, we used the *I*-band images from Grouchy (2008) to derive Q_g values, while for the CBB96 sample, we used narrowband red continuum images. In spite of being narrowband, the CBB96 images were deep enough to be useful for this purpose. The derivation of Q_g requires an estimate of the scale height, h_z , of the vertical density distribution. We assumed an exponential vertical density distribution, although this choice has little impact on the results. The scale height h_z is not directly observable for any of our galaxies (CBB96 or this paper). Instead, we must infer a value from the radial scale length h_r . For the combined barred/nonbarred sample, radial scale lengths were derived using the bulge/disk/bar (“bdbar”) two-dimensional decomposition code described by Laurikainen et al. (2005). Parameters and descriptions of the decompositions for the Table 1 galaxies are discussed in a separate paper (Grouchy 2008). For the CBB96 sample, we only summarize our fitted radial scale lengths. De Grijs (1998) showed that vertical scale heights scale in a type-dependent manner with radial scale length, the ratio h_z/h_r decreasing with later Hubble types. For types Sa and earlier, $h_z/h_r \approx 1/4$; types Sab to Sbc, $h_z/h_r \approx 1/5$; and types Sc and later, $h_z/h_r \approx 1/9$. Laurikainen et al. (2005) show that the largest source of error in the measurement of Q_g comes from the assumption of the disk scale height, which can be as high as $\pm 8\%$ to $\pm 20\%$.

and easily overshadows errors from orientation parameters (see Laurikainen et al. 2005 for details of error analysis). Figure 15 shows the ratio map and $Q_T(r)$ profile for four barred galaxies from the CBB96 sample.

Table 8 summarizes our force calculation results. In addition to Q_g and Q_r , the $m = 2$ Fourier component at the ring radius (denoted as A_{2r}), and the radius where Q_g occurs (denoted as $r(Q_g)$), are also compiled. Table 9 summarizes the same parameters for 27 of the CBB96 galaxies. The radial scale lengths listed in both tables come from one-dimensional and two-dimensional decompositions. The full details of the two-dimensional decompositions will be presented in a separate paper. For our present purposes, we compared the two-dimensional derived disk scalelengths with those derived from a one-dimensional fit and chose the best fit. The galaxies which have one-dimensional fitted scale lengths are noted in the tables. The value of Q_g for the combined sample ranges from ≈ 0.04 to 0.55.

5. Rings and Galaxy Properties

5.1. Ring Star Formation Rates

The data in Tables 1, 2, 6 – 9 provide a sample of 44 unique galaxies: 26 nonbarred or slightly barred (SA or SAB) and 18 more strongly barred (SAB, SAB, or SB) galaxies. Figure 16 examines correlations between the SFRs of the inner rings and various galaxy parameters. Three of the galaxies listed in Table 1 are also included in the CBB96 sample of Table 2, so we use the average values for these cases. The open squares in these plots correspond to the SA galaxies; asterisks represent the SAB galaxies; and the solid points correspond to the SB galaxies. The solid line included in each graph represents the "Ordinary Least Squares bisector" (OLS bisector) linear fit to the data as derived by the program SLOPES (Isobe et al. 1990). Using the OLS bisector was recommended by Isobe et al. when the errors of the data on both axes are either unknown or only vaguely known.

To test for any correlations, we used the Spearman's rank correlation coefficient which measures the strength of the relationship between two parameters by assigning a number ranging between $\rho = -1$ and $+1$. A rank correlation coefficient of -1 is considered a perfect anti-correlation; a value close to 0 means no correlation is found; and a value close to $+1$ is considered a strong positive correlation. A non-parametric test quantity (i.e. rank correlation rather than Pearson's linear correlation coefficient) was chosen, in order to avoid making any assumptions about the unknown distributions of the compared quantities, or about the exact functional form of the correlation: note that the rank correlation coefficient between $\log(y)$ and $\log(x)$ is exactly the same as that between x and y .

In addition to the rank correlation coefficient, the significance was calculated to establish the reliability of the relationship. For this paper, we adopted the following convention: a significance less than 0.05 is the maximum value to be considered significant, and a value less than 0.01 is classified as very significant.

Figure 16(a) compares the absolute blue magnitude normalized to the Galaxy's luminosity to the SFR of the inner ring. The barred and nonbarred galaxies cover approximately the same range in M_B^0 , and no correlation was found between the two parameters.

Figure 16(b) shows the relationship of the SFR of the galaxy's inner ring to the de Vaucouleurs type index. The plot shows a larger spread in the SFR values toward higher index values, and the parameters have a correlation of $\rho = 0.38$ with a significance of 0.02.

In Figure 16(c), we search for any dependence between the SFR and the relative size of the inner ring.

The parameter r_{dep}/h_r is the deprojected semimajor axis radius of the ring relative to the fitted radial scale length. There is a suggestion in the plot that relatively smaller rings have higher SFRs; however, no significant correlation was found between the two parameters.

In Figure 16(d), the inner ring SFRs are compared with the deprojected H α ring axis ratios, q_{dep} . The deprojections for the present paper’s sample used orientation parameters from Grouchy (2008), while those for the CBB96 sample are from Table 4 of CBB96. The issue of ring axis ratio is significant because CBB96 showed that the distribution of HII regions around inner rings is sensitive to ring shape but not necessarily to Q_g . The rounder nonbarred galaxy rings in our sample have a higher average SFR compared to the barred galaxy rings of similar shape. For example, the relatively circular inner ring of NGC 6935 from CBB96 has a higher SFR than all of the CBB96 barred galaxies. In our present sample, the extremely luminous galaxy ESO 231–1 has the highest estimated ring SFR and is also a case where the inner ring is relatively circular. In general, however, no significant correlation between the inner ring SFRs and the ring shape was found.

In Figure 16(e) and 16(f), the inner ring SFRs are compared with Q_r and Q_g , respectively, and no significant correlation is found in either case. It is generally accepted that bars are efficient at collecting gas near major resonances, such as outer Lindblad resonance (OLR), ILR, and the inner 4:1 resonance (UHR), based on the early sticky-particle models of Schwarz (1981; 1984a; 1984b) and subsequent follow-up papers (e.g., Byrd et al. 1994; Rautiainen & Salo 2000). More recent studies have suggested that resonances are less of an issue, and that “orbit transition regions” (Regan & Teuben 2004) or “invariant manifolds” (Romero-Gómez et al. 2006, 2007) are better physical ways of describing rings. In all of these interpretations, however, it is expected that stronger bars will have a greater impact on gas flow and collecting material into rings than would weaker bars.

In the classical resonance interpretation of inner rings, as material is funneled inward to the ILR, some of the gas will collect and remain in the UHR (see, e.g., Simkin et al. 1980). An inner ring will form in this location if the bar strength near the UHR is strong enough to trigger shocks in the area (see review of Buta & Combes 1996). Compared to the ILR, the UHR is considered a relatively weak resonance, and some of the gas will leave the inner ring to settle in the nuclear ring. In order to have continual star formation in an inner ring, the gas must be replenished either through gas released through stellar evolution, by the continued effects of the bar, or by external gas accretion (Bournaud & Combes 2002). If the bar weakens, we would expect the rate at which the material moves inward to lessen, resulting in an eventual drop in a ring’s SFR. However, we find that there is not a significant correlation between the strength of the bar torque and the inner ring SFR of our sample. The limitations of our sample may make it difficult to detect such an effect, but it is also clear that other factors besides bar strength must be involved in ring star formation, such as the amount of gas in the ring region. For example, it is interesting that NGC 7267, which has the strongest bar in the sample, has only a weak, mostly open inner pseudoring. In this case, most of the H α emission is confined to the bar itself. Therefore, without a complete view of the SFR history and gaseous content of our sample, it is difficult to draw any strong conclusions from the lack of correlation between the ring SFR and the bar torque strength.

5.2. Ring Axis Ratios

From current theories of galaxy dynamics, we would expect *inner rings* to be more elongated in strongly barred galaxies than in weakly-barred ones (e.g, Salo et al. 1999; Schwarz 1985). However, Buta (2002) used the CBB96 sample to show that intrinsic inner ring shape does not depend strongly on bar strength

as defined by the parameter Q_g . This was based on preliminary derivations of Q_g and a few of the more exceptional examples, such as UGC 12646 and NGC 6782 as barred galaxies with exceptionally elongated rings, and NGC 53 and NGC 7329 as similar cases with much rounder rings. Here we approach the issue differently by using a larger sample as well as a newly defined parameter Q_r . Figure 17 shows plots of deprojected ring axis ratio q_{dep} versus Q_g and Q_r , separating galaxies by family classification (SA, SAB, SB) and by ring type (inner, outer).

When the deprojected axis ratio for all rings in the sample is plotted against Q_g , no correlation is found (see Figure 17(a)). However, when we compare the deprojected ring shape to Q_r , we find a correlation of $\rho = -0.33$ and a significance of 0.005 (see Figure 17(c)). When focussing on only the *inner* rings, we find that both Q_g and Q_r correlate significantly with the ring shape (see Figure 17(b) and Figure 17(d), respectively). For Q_g , we find a correlation of $\rho = -0.42$ with a significance of 0.007, and for Q_r , we find a correlation of $\rho = -0.41$ with a significance of 0.008. Therefore, we are able to say that while inner rings appear to be affected by Q_g , outer rings are not. This is obvious by looking at the correlation of ring shape with Q_r : the bar induced tangential force is significant at the position of the inner ring, but not at the distance of the outer ring.

A greater insight into what is driving ring shape can be gained by restricting the analysis to the barred galaxies. The reason for doing this is that we see round and highly elongated inner rings in strongly barred galaxies, and including nonbarred galaxies could confuse the possible reason for this. Figure 18 shows q_{dep} versus Q_g and Q_r for the inner rings of 19 CBB96 galaxies having $Q_g \geq 0.15$. Several galaxies are highlighted, including the four best cases (NGC 53, 6782, 7329, and UGC 12646) of round versus elliptical SB inner rings from Buta (2002). In addition, Figure 18(a) shows q_{dep} versus the *relative forcing* Q_r/Q_g . While there is little correlation between q_{dep} and Q_g or Q_r (Figures 18(b) and 18(d)) individually for this subsample, Figure 18(a) shows a strong correlation of $\rho = -0.63$ with a significance of 0.002 between q_{dep} and Q_r/Q_g . The two discrepant points, NGC 1832 and 7267, may depart the correlation for different reasons. NGC 1832 has a dominant spiral and a relatively weak bar, unlike most of the other galaxies, and although NGC 7267 has the strongest bar in the sample, it also has the weakest inner ring, a highly elongated, open pseudoring with an ill-defined major axis radius. For the remaining 17 galaxies, Figure 18(a) shows that the most elongated inner rings are found in galaxies having $Q_r/Q_g \approx 1$, while the roundest inner rings are found in galaxies having $Q_r/Q_g \approx 0.5$. This suggests that *the key factor determining ring shape in the presence of a significant bar is the location of the ring relative to the bar maximum*. This is schematically illustrated in Figure 19 using NGC 53 and NGC 6782 as examples. When r_{dep} is close to $r(Q_g)$, the ring lies essentially on top of the bar and can be highly elongated, even if Q_g is relatively weak (as in NGC 6782 and IC 1438). But when r_{dep} is well outside $r(Q_g)$, the ring has formed far enough from the bar maximum that it can be quite round, even if Q_g is relatively strong (as in NGC 53 and 7329). These effects are manifested in the forcing ratio Q_r/Q_g .

Figures 18(c), 18(e), and 18(f) show other correlations for the same subset of galaxies. Figure 18(c) shows that of the four labeled galaxies, the two with the most elliptical inner rings have the highest blue luminosity. The two with the most circular inner rings are 0.5–1 mag fainter than these. There is no significant correlation between q_{dep} and the blue luminosity. Figure 18(e) shows q_{dep} versus the CBB96 ring star formation distribution parameter F_2 , defined as the relative amplitude of the $m = 2$ Fourier component of the $H\alpha$ distribution around the rings. F_2 is taken from Figure 15 of CBB96 and shows a similar correlation with q_{dep} for the $H\alpha$ distribution as for the continuum ring light (Figure 16 of CBB96). As expected from Figure 18(a), F_2 roughly increases with increasing Q_r/Q_g .

5.3. Other Correlations

Figure 20 shows several plots using the equivalent width, W_λ , of the $\text{H}\alpha + [\text{NII}]$ emission instead of the SFR. W_λ conceivably could give a different view of ring star formation. Figure 20(a) shows the relationship between the galaxy-wide $\text{H}\alpha + [\text{NII}]$ equivalent width and Q_g . This plot includes the Table 1 sample and did not result in any correlation. Our values of the galaxy-wide equivalent width are comparable to those found by Hameed & Devereux (1999) for another sample of early-type galaxies. Figures 20(b) and 20(c) show the relationship between the equivalent width of $\text{H}\alpha + [\text{NII}]$ emission from the inner ring to Q_r and q_{dep} , respectively. No significant correlation was found in either case.

Kennicutt (1983) showed that there is a correlation between $\log W_\lambda$ and the corrected total color index, $(B - V)_T^c$ of normal galaxies. The correlation can be tied to properties of the initial mass function, or IMF. Figure 20(d) shows the same plot for our combined barred/nonbarred galaxy sample, using RC3 colors for the CBB96 sample and measured colors from Grouchy (2008) for the Table 1 sample. The latter were corrected for Galactic extinction, tilt, and redshift using RC3 prescriptions. As Kennicutt found, the bluer galaxies in our sample have larger $\text{H}\alpha + [\text{NII}]$ equivalent widths with a strong correlation of $\rho = -0.77$ and a significance ≤ 0.0001 .

Figure 21(a) looks at the relationship between the semimajor axis of the deprojected inner ring, r_{dep} , and the radius at which Q_g is measured, both in arcseconds. There is a slight spread in the values of r_{dep} and $r(Q_g)$, but a correlation was detected with $\rho = 0.27$ and a significance 0.02. Further investigation indicates that this relationship is due to the strongly barred SB galaxies which have a correlation of $\rho = 0.57$ and a significance 0.003. Typically, the length of a bar is greater than or equal to the location of Q_g (see Laurikainen et al. 2004 Figure 5; also Buta et al. 2009, Section 7). The location of an inner ring is typically thought to be related to the UHR (Rautiainen & Salo 2000) whereas a self-sustained bar does not extend beyond the radius of corotation (Contopoulos 1980; but see Zhang & Buta 2007 and Buta & Zhang 2009). Our data show that the ratio of r_{dep} to $r(Q_g)$ is greater than unity for the barred galaxies in the sample (see Figure 21(a)). Therefore, as expected, the rings in these barred galaxies lie at a radius larger than the radius of Q_g and the radius of the bar. For nonbarred galaxies the correlation disappears, and the relationship becomes mostly random.

The last two panels of Figures 21 compare the $m = 2$ Fourier amplitude at the position of the ring with Q_g (see Figure 21(b)) and Q_r (see Figure 21(c)). While the amplitude range is the same in both plots, the values of Q_g have a wider spread than those of Q_r . This spread appears to be attributed to the strongly barred galaxies of the sample which have Q_g ranging from 0.2 to 0.6 and Q_r ranging from 0.05 to 0.26. At the same time, for nonbarred galaxies, Q_r and Q_g both range between 0 and 0.2 due to the lack of a strong bar. Since rings are usually located just outside the ends of a strong bar, we would expect Q_r to be, on average, lower than Q_g for barred galaxies. Even with these differences, both Q_g and Q_r are strongly correlated with the $m = 2$ amplitude.

6. Discussion

6.1. Evolving Ringed Barred Galaxies

The dynamical theory of ring formation in the context of bar resonances is reviewed by Buta & Combes (1996). In simulations, rings form by gas accumulation at specific resonances, owing to gravity torques from the bar pattern. The gas settles into a main periodic orbit near the resonance that does not cusp or cross

another orbit. There is no net torque on the orbit, so that any further evolution of the ring will involve mainly how it forms stars, how its sharpness will change over time as ring stars age, and, in principle, how the bar itself (pattern speed, strength) may change over time. In an equilibrium situation, a ring will be aligned either parallel or perpendicular to the bar. Rings should form stars as long as gas is available and presumably above a certain threshold of surface density, and gas should be gathered smoothly as long as the bar exists. A recent simulation of a classical ringed barred galaxy is given by Treuthardt et al. (2008).

Given this basic scenario, a few questions arise: how does the time lag between the gathering of gas into a resonance region and the onset of star formation compare with the evolutionary timescale of the bar? Once the bar has dissolved, how long does it take for the star formation in the ring to cease? And, finally, once the bar has dissolved and star formation in the ring has ceased, how long can the ring persist as a visible ring-like feature? These questions are relevant because bar dissolution is one possible explanation for rings in nonbarred galaxies. We can make some judgments based on published models.

The dissolution of a bar by the buildup of a CMC was considered by Hasan & Norman (1990), who showed that such an object would cause chaos in bar-supporting orbits near the center. If the mass of this object increased such that the ILR reached the ends of the bar, then the bar would be destroyed. Shen & Sellwood (2004) reconsidered the problem by determining not only how massive but also how dense a CMC needs to be to dissolve a bar. Their conclusion was that a CMC would not, in most galaxies, have the mass or central density needed to dissolve bars.

Bournaud & Combes (2002) developed models where the flow of gas to the center, driven by a bar, builds up the central mass sufficiently to destroy the bar. But they also considered how external gas accretion might prevent total bar destruction and even lead to bar regeneration after the end of a previous major bar episode. In the presence of gas accretion, a galaxy could be seen as barred for most of its lifetime. Depending on model details, a galaxy may have one or more bar episodes during a Hubble time. Even in the absence of accretion, a galaxy can appear as barred for up to 2Gyr, before dissolving into an oval lens. We can argue based on such models that in a worst-case scenario, a bar may last only for 1Gyr. Bar development depends on model parameters. For example, Rautiainen & Salo (2000) show two-dimensional n -body models with variable Toomre stability parameter, Q . Considering Q ranging from 1.25 to 2.5, they found that bars formed quickly for low Q values and much more slowly or not at all for the high Q values.

Test-particle simulations with an analytical bar and disk (e.g., Simkin et al. 1980; Schwarz 1981, 1984a; Byrd et al. 1994) have provided insights into the timescales of ring formation, usually in units of the bar rotation period. For a galaxy of absolute blue magnitude -20.4 , a characteristic rotation speed is 250 km s^{-1} , based on the B -band Tully-Fisher relation of Yasuda et al. (1997). A typical inner ring in our sample has a radius of 6 kpc, and if we assume a flat rotation curve and that the inner ring lies near the inner 4:1 ultraharmonic resonance, this would give a typical bar rotation period of $2 \times 10^8 \text{ yr}$. The cited papers show that gaseous inner rings may form in 3 – 7 bar rotations (0.6 – 1.4 Gyr), and gaseous outer rings in 10 – 20 bar rotations (2 – 4 Gyr), for a bar turned on fully in about two bar rotations.

The Rautiainen & Salo (2000) models also used test particles for gas, but for the stellar component, an n -body treatment was used, therefore the bar formed from a natural instability. The timescales for the rings were found to depend on the timescales for the bar, but once the bar formed, ring formation timescales thereafter were similar to those from the analytical models.

Given these approximate timescales, is it possible that a bar could gather gas into a resonance region over some period of time, and then dissolve *before* the ring is seen as an active star-forming zone, giving us a nonbarred ringed galaxy with a ring SFR comparable to that of a barred ringed galaxy? Tamburro

et al. (2008) have considered the time lag between the densest HI gaseous phase and the initial massive star formation phase in spiral arms based on a comparison between HI and 24 μm emission peaks in a sample of spiral galaxies. They concluded that this time lag is fairly rapid, on the order of 1 – 4 Myr. If we consider that, in simulations, rings usually begin as pseudorings made of wrapped spiral arms, then a similar timescale may be relevant to the HI \rightarrow 24 μm conversion in rings. From this, we suggest that, after the bar has dissolved, it is unlikely that significant star formation will suddenly turn on in a ring because of a long time lag, which would have to be on the order of a Gyr for such a scenario to work. It is most likely that star formation in a ring will begin when the bar is strong, because that is when the bar will be most effective at gathering gas into resonant regions. How long the star formation proceeds in the absence of the bar will depend on the star formation efficiency.

The case of NGC 7702 suggests that a ring may experience a rapid burst of star formation, and then evolve in a quiescent manner for a long time afterward. Buta (1991) isolated the bright inner ring of NGC 7702 from its surrounding background old disk light, and found that the net colors are consistent with a “star formation cutoff” model where the star formation proceeds uniformly for 10^7 yr, and then cuts off (Larson & Tinsley 1978). The observed net colors suggest that star formation ended in the ring 1 – 2 Gyr ago, which may be long enough for a primary bar to dissolve in that case. Our H α imaging confirms the lack of any recent star formation in either of the rings of NGC 7702. In contrast to the ring colors, the colors of the background star light at the ring position are consistent with those of a normal S0⁺ galaxy having a monotonically declining SFR. NGC 7702 may be the kind of “nonbarred” ringed galaxy we might expect from bar dissolution. Even so, the galaxy is not completely unbarred. As we have noted, it has a small nuclear bar and its bright inner ring is an intrinsically oval, bar-like feature.

Athanassoula (1996) has shown that the morphology of a galaxy like NGC 7217 can be explained in terms of a dissolved bar model. In her model, a bar is turned on after two bar rotations, and then is completely turned off by 12 bar rotations. While the bar is present, the galaxy forms an R_2' outer pseudoring that evolves to a more detached feature. The ring is initially slightly elongated, but becomes more circular once the bar is gone. Interestingly, the ring persists for more than 20 additional bar rotations, only becoming more diffuse with time. The model does not tell us how long star formation in the ring might proceed, but as long as the ring remains a region of enhanced gas density (which it is in the model), it will probably form stars. This model suggests that star formation may proceed in a ring for as long as 2 – 4 Gyr after the bar has dissolved. Our H α image of NGC 7217 shows that the outer ring is where most of the HII regions are found, and Buta et al. (1995) also found the ring to be a concentration of HI gas. The authors derived the net colors of the outer ring of NGC 7217 and found that they lie essentially on the normal galaxy sequence, consistent with a roughly uniform SFR for most of the lifetime of the galaxy. Although this result is very different from NGC 7702, NGC 7217 could still be another example of a nonbarred ringed galaxy that evolved from a former barred ringed galaxy.

6.2. Star Formation Triggering in Rings

One of our main goals in this paper was to examine how important a bar might be in triggering the star formation seen in inner rings. That is, does the presence of a strong bar enhance star formation in a normal inner ring? For our limited sample, the range of SFRs for barred and nonbarred galaxy inner rings is similar. For a similar range in absolute blue magnitudes, the average inner ring SFR for rounder nonbarred galaxy rings is actually higher than for barred galaxy rings of similar shape (Figure 16(d)). This suggests that while a bar may be capable of concentrating star formation in an inner ring, it does not increase the overall

efficiency of star formation in such a ring. This may not be true for nuclear rings, where the star formation efficiency can be comparatively high (e.g., Schinnerer et al. 1997) and enhanced nuclear star formation can cause correlations between IRAS flux ratios and bar strength and length (Martinet & Friedli 1997). Our result for bars and inner rings is very similar to what McCall & Schmidt (1986) and Elmegreen & Elmegreen (1986) concluded concerning the impact of spiral density waves on global SFRs (Kennicutt 1998b). Both studies concluded that density waves are not the main triggers of star formation in galaxies.

Although our combined sample cannot be considered statistical, this result is consistent with other previous studies. Moss & Whittle (1993) found no difference in detected $H\alpha$ emission between barred and nonbarred galaxies in cluster and field samples. Tomita et al. (1996) found no significant differences in the far-infrared to blue flux ratio, an indicator of the current SFR, between samples of barred and nonbarred spirals of types Sa, Sb, and Sc. They concluded that an optical bar structure has no impact on present-day star formation activity in galaxies. In contrast to this, Devereux (1987) showed that $10\mu\text{m}$ luminosities are definitely higher for early-type barred galaxies than in nonbarred early types or late types.

Hameed & Devereux (1999) also studied the $H\alpha$ emission for a sample of early-type galaxies, including several with strong rings. In addition to showing enhanced star formation in the rings, these authors found that some early-type galaxies have a rate of massive star formation comparable to Sc galaxies. Hameed & Young (2003) also showed that galactic interactions can have a significant effect on the current SFR in many early-type galaxies.

An alternative interpretation of the lack of correlation between bar strength and ring SFR in our sample could simply be sample inhomogeneity. Some galaxy rings have formed in response to a bar, while others have formed via a different mechanism, so that the ring SFRs may depend on different factors. (See for example, Struck (2009), for an interpretation of our sample galaxy ESO 236–29 in terms of analytical collisional ring galaxy theory.) Also, the sample may include a mix of rings in different evolutionary states. Martinet & Friedli (1997) interpreted four classes of star formation activity among late-type barred spirals in terms of possible evolutionary paths including the age of the bar.

6.3. Ring Star Formation and Intrinsic Ring Shape

The intrinsic shape (q_{dep}) of the ring appears to affect the star formation process in rings more than does the maximum strength (Q_g) of the bar. Nonbarred galaxy rings tend to be round, and HII regions distribute fairly randomly around them. The same is true for a round barred galaxy inner ring. But significant intrinsic elongation causes HII regions to bunch up around the bar axis. If, in an equilibrium situation, gas circulates around the ring as if it is a periodic orbit, then clouds will spend more time near the ring major axis points (around the bar ends) than they will near the ring minor axis points (Contopoulos 1979). Byrd et al. (2006) argue that velocity perturbations in the inner ring of NGC 3081 due to its extreme elongated shape can explain the concentrated star formation in the ring major axis regions. In this case, crowding, rather than spiral shock fronts, might explain the HII region bisymmetry. Not only is the HII region distribution in NGC 3081 affected by the ring shape, but also the luminosity function of young clusters is affected in that more luminous clusters are found near the bar major axis (e.g., Buta et al. 2004). Byrd et al. (2006) argue that clusters in the inner ring of NGC 3081 show a position-age sequence suggesting that they form around the bar ends and move further upstream along the ring away from the bar ends. In spite of the clear shape effects, when total ring SFR are considered, there is little dependence on q_{dep} in our small sample.

Our new sample has allowed us to look into the relationship between ring shape, bar strength, and star

formation properties. Buta (2002) had shown that for barred galaxies, there is little correlation between q_{dep} and Q_g , which acts as a good approximation to the bar strength. By adding in our new sample of nonbarred galaxy inner rings, some correlation between q_{dep} and Q_g is now found. However, for the whole sample, a better correlation is found between q_{dep} and the maximum relative forcing at the ring major axis radius, Q_r . Thus, at some level, Q_r is a more important controlling parameter for ring shape than is Q_g . Nevertheless, we have shown that for inner rings in barred galaxies having $Q_g \geq 0.15$, the more likely controlling parameter for ring shape is Q_r/Q_g . When this ratio is close to unity, SB inner rings tend to be highly elongated, while when significantly less than unity, SB inner rings tend to be rounder. Weaker correlations are found between q_{dep} and Q_g and Q_r for this more restricted subsample. As bar strength decreases, the ratio Q_r/Q_g becomes ill-defined and subject to noise or other nonaxisymmetric features, such as spirals. The correlation between q_{dep} and Q_r/Q_g indicates that indeed, on some level, a bar does play a role in ring star formation. This is because Q_r/Q_g determines q_{dep} , which in turn affects how ionized gas is distributed in the inner ring. Yet, with our small samples, we have not been able to uncover a connection between the rate of star formation in inner rings and either the nonaxisymmetric torque strength or the ring shape.

7. Conclusions

Our study, based on a combined sample of 26 nonbarred or weakly barred galaxies and 18 strongly barred galaxies, has led to the following conclusions:

1. Rings in nonbarred galaxies are often well-defined, narrow zones of HII regions and H α emission. This is consistent with the enhanced blue colors seen in broadband images, indicating that the rings are well-organized, active zones of star formation, a trait which is very much in common with the more abundant rings seen in barred galaxies (CBB96). The best examples we illustrate here are found in ESO 111–22, ESO 198–13, ESO 231–1, ESO 236–29, ESO 526–7, IC 1993, NGC 7020, NGC 7187, NGC 7217, and NGC 7742.
2. For the 20 ringed galaxies illustrated in this paper, azimuthally averaged H α surface brightness profiles follow the approximate shape of B -band azimuthally averaged profiles. This is in contrast to the finding of Ryder & Dopita (1994) that H α profiles have a longer radial scale length than optical V or I -band profiles.
3. The organized nature of the H α emission from rings allows us to define the rings well enough to selectively integrate the fluxes and estimate SFRs *for the rings alone*. Combining our sample of 20 nonbarred ringed galaxies with a larger sample of ringed and mostly barred galaxies from CBB96, we were able to investigate possible correlations between ring SFRs and bar strength. The analysis showed that for a typical ringed galaxy having an absolute blue magnitude of ≈ -20 , inner ring SFRs show little or no dependence on the strength of the nonaxisymmetric perturbation. There are galaxies showing exceptional star-forming rings with little or no trace of a bar. The few outer rings in the sample are consistent with the results from the inner rings.
4. Our combined sample allowed us to further investigate the correlation, if any, between bar strength and intrinsic inner ring shape. A previous study (Buta 2002) had suggested that inner ring shape did not depend on bar strength as defined by Q_g . Galaxies having similar values of Q_g can have very different values of q_{dep} (see, for example, Buta et al. 2007). When our sample of nonbarred ringed galaxies is considered, some correlation with Q_g is found. However, a better correlation is found when a newly defined parameter, the maximum relative torque at the position of the ring, Q_r , is used. This is in agreement with the results from numerical simulations, and implies that the metric properties of the rings are dictated by the local bar strength.

5. For barred galaxies having $Q_g \geq 0.15$, a better correlation is found between q_{dep} and Q_r/Q_g than between q_{dep} and Q_r . For barred galaxies, this suggests that the controlling parameter for inner ring shape is the location of the ring relative to the bar maximum. If the ring major axis radius is at $\approx 1.4r(Q_g)$, an inner ring can be nearly circular, while if the ring major axis radius is at $\approx 1.1r(Q_g)$, the ring is practically on top of the bar and is highly elongated. Q_r/Q_g loses its usefulness when a bar is weak or absent.

6. The combined barred/nonbarred sample includes some intrinsically very large rings. A comparison of the deprojected linear diameters of inner rings in our sample with an earlier analysis of nearby galaxies by Buta & de Vaucouleurs (1982) shows that the average nonbarred ring diameters are comparable to those of the barred galaxies. In the Buta & de Vaucouleurs analysis, SA inner rings averaged a factor of 2 smaller than SB inner rings. The emphasis on large SA rings in our sample is not unexpected because of the way the sample was selected.

7. We verify previous analyses which have shown that nonbarred ringed galaxies are a diverse and relatively inhomogeneous class of objects whose ring formation mechanisms are likely varied. Evolved bar resonance rings, spiral density wave resonance rings, interaction-produced rings, and even the limitations of B -band images for recognizing bars could account for most of the features observed in our combined sample.

R.G. and R.B. have been supported by NSF grant AST 050-7140 to the University of Alabama. R.G. is now supported by an NSF International Research Fellowship (OISE-0852959). E.L., H.S., and R.G. acknowledge the support of the Academy of Finland. This research has made use of the NED, which is operated by the Jet Propulsion Laboratory, California Institute of Technology, under contract with NASA. We thank Drs. Françoise Combes, Lia Athanassoula, Patrick Treuthardt, and the anonymous referee for their helpful comments. We also thank NOAO and CTIO for use of the 1.5 m telescope.

REFERENCES

- Athanassoula, E. 1996, in ASP Conf. Ser. 91, Barred Galaxies, ed. R. Buta, D.A. Crocker & B. G. Elmegree (San Francisco, CA: ASP), 309
- Athanassoula, E., Romero-Gómez, M., & Masdemont, J. J. 2009, MNRAS, 394, 67
- Block, D. L., Bournaud, F., Combes, F., Puerari, I., & Buta, R. J. 2002, A&A, 394, L35
- Bournaud, F. & Combes, F. 2002, A&A, 392, 83
- Bournaud, F., Combes, F., & Semelin, B. 2005, MNRAS, 364, L18
- Buta, R. J. 1988, ApJS, 66, 233
- Buta, R. J. 1990a, ApJ, 354, 428
- Buta, R. J. 1990b, ApJ, 356, 87
- Buta, R. J. 1991, ApJ, 370, 130
- Buta, R. J. 1995, ApJS, 96, 39 (CSRG)
- Buta, R. J. 2002, in ASP Conf. Ser. 275, Disks of Galaxies: Kinematics, Dynamics, and Perturbations, ed. E. Athanassoula, A. Bosma, & R. Mujica (San Francisco, CA: ASP), 185
- Buta, R. J. & Block, D. L. 2001, ApJ, 550, 243
- Buta, R. J., Byrd, G. G., & Freeman, T. 2003, AJ, 125, 634
- Buta, R. J., Byrd, G. G., & Freeman, T. 2004, AJ, 127, 1982
- Buta, R. J. & Combes, F. 1996, Fund. Cosmic Phys, 17, 95
- Buta, R. J., Corwin, H. G., & Odewahn, S. C. 2007, The de Vaucouleurs Atlas of Galaxies, Cambridge, Cambridge University Press
- Buta, R. J. & Crocker, D. A. 1991, AJ, 102, 1715
- Buta, R. J. & Crocker, D. A. 1993, AJ, 105, 1344
- Buta, R. J., Crocker, D. A., & Byrd, G. G. 1992, AJ, 103, 1526
- Buta, R. J. & de Vaucouleurs, G. 1982, ApJS, 48, 219
- Buta, R. J., Knapen, J., Elmegreen, B., Salo, H., Laurikainen, E., Elmegreen, D., Puerari, I., & Block, D. L. 2009, AJ, 137, 448
- Buta, R. J. & Zhang, X. 2009, ApJS, 182, 559
- Buta, R. J., van Driel, W., Braine, J., Combes, F., Wakamatsu, K., Sofue, Y., et al. 1995, ApJ, 450, 593
- Byrd, G. G., Freeman, T., & Buta, R. J. 2006, AJ, 131, 1377
- Byrd, G. G., Rautiainen, P., Salo, H., Buta, R. J., & Crocker, D. A. 1994, AJ, 108, 476
- Casasola, V., Combes, F., Garcá-Burillo, S., Hunt, L. K., Lón, S., & Baker, A. J. 2008, A&A, 490, 61
- Combes, F. & Sanders, R. H. 1981, A&A, 96, 164
- Contopoulos, G. 1979, in Photometry, Kinematics, & Dynamics of Galaxies, ed. D. S. Evans (Austin, TX: Univ Texas Press), 425
- Contopoulos, G. 1980, A&A, 81, 198
- Crocker, D. A., Baugus, P. D., & Buta, R. J. 1996, ApJS, 105, 353 (CBB96)
- de Grijs, R. 1998, MNRAS, 299, 595

- de Vaucouleurs, G. & Bollinger, G. 1979, *ApJ*, 233, 433
- de Vaucouleurs, G. & Buta, R. J. 1980, *AJ*, 85, 637
- de Vaucouleurs, G., de Vaucouleurs, A., Corwin, H., Buta, R. J., Paturel, G., & Fouqué, P. 1991, *Third Reference Catalog of Bright Galaxies* (New York: Springer) (RC3)
- de Zeeuw, P. T., Bureau, M., Emsellem, E., Bacon, R., Carollo, C., Copin, Y., et al. 2002, *MNRAS*, 329, 513
- Devereux, N. 1987, *ApJ*, 323, 91
- Donovan, J. L., et al. 2009, *AJ*, 137, 5037
- Elmegreen, B. G. & Elmegreen, D. M. 1986, *ApJ*, 311, 554
- Finn, R. A., Zaritsky, D., & McCarthy, D. W., Jr. 2004, *ApJ*, 604, 152
- Friedli, D. & Pfenniger, D. 1991, in *IAU Symp*, 146, *Dynamics of Galaxies and Their Molecular Cloud Distributions*, ed. F. Combes & F. Casoli (Dordrecht: Kluwer), 362
- Grouchy, R. D. 2008, PhD dissertations, Univ. Alabama
- Grouchy, R. D., Buta, R. J., Salo, H., Laurikainen, E., & Speltincx, T. 2008, *AJ*, 136, 980 (Paper 1)
- Hameed, S. & Devereux, N. 1999, *AJ*, 118, 730
- Hameed, S. & Young, L. M. 2003, *AJ*, 125, 3005
- Hamuy, M., Walker, A. R., Suntzeff, N. B., Gigoux, P., Heathcote, S. R., & Phillips, M. M. 1992, *PASP*, 104, 533
- Hasan, H. & Norman, C. A. 1990, *ApJ*, 361, 69
- Howarth, I. D. 1983, *MNRAS*, 203, 301
- Isobe, T., Feigelson, E. D., Akritas, M. G., & Gutti, J. B. 1990 *ApJ*, 364, 104
- Jacoby, G. H., Quigley, R. J., & Africano, J. L. 1987, *PASP*, 99, 672
- Kennicutt, R. C. 1983, *ApJ*, 272, 54
- Kennicutt, R. C. 1998a, *ApJ*, 498, 541
- Kennicutt, R. C. 1998b, *ARA&A*, 36 189
- Kennicutt, R. C. & Kent, S. M. 1983, *AJ*, 88, 1094 (KK83)
- Kennicutt, R. C., Tamblyn, P., & Congdon, C. W. 1994, *ApJ*, 435, 22
- Kohoutek, L., & Martin, W. 1981, *A&AS*, 44, 325 (KM81)
- Koopmann, R. A. & Kenney, J. D. P., 2006, *ApJS*, 162, 97
- Kormendy, J. 1979, *ApJ*, 227, 714
- Larson, R. B. & Tinsley, B. M. 1978, *ApJ*, 219, 46
- Laurikainen, E. & Salo, H. 2002, *MNRAS*, 337, 1118
- Laurikainen, E., Salo, H., & Buta, R. J. 2005, *MNRAS*, 362, 1319
- Laurikainen, E., Salo, H., Buta, R. J., & Vasylyev, S. 2004, *MNRAS*, 355, 1251
- Madore, B. F., Nelson, E. & Petrillo, K. 2009, *ApJS*, 181, 572
- Mark, J. W. K. 1974, in *IAU Symp*. 58, *The Formation and Dynamics of Galaxies*, ed. J. R. Shakeshaft (Dordrecht: Reidel), 417

- Martinet, L. & Friedli, D. 1997, *A&A*, 323, 363
- McCall, M. L. 1986, *PASP*, 98, 992
- McCall, M. L. 2004, *AJ*, 128, 2144
- McCall, M. L. & Schmidt, F. H. 1986, *ApJ*, 311, 548
- Moss, C. & Whittle, M. 1993, *ApJ*, 407, L17
- Pogge, R. W. 1989, *ApJ*, 345, 730
- Rautiainen, P. & Salo, H. 2000, *A&A*, 362, 465
- Regan, M. & Teuben, P. 2004, *ApJ*, 600, 59
- Romanishin, W. 1990, *AJ*, 100, 383
- Romero-Gómez, M., Athanassoula, E., Masdemont, J. J., & García-Gómez, C. 2007, *A&A*, 472, 63
- Romero-Gómez, M., Masdemont, J. J., Athanassoula, E., & García-Gómez, C. 2006, *A&A*, 453, 39
- Ryder, S. & Dopita, M. A. 1994, *ApJ*, 430, 142
- Salo, H., Rautiainen, P., Buta, R. J., Purcell, G. B., Cobb, M. L., Crocker, D. A., & Laurikainen, E. 1999, *AJ*, 117, 792
- Salpeter, E. E. 1955, *ApJ*, 121, 161
- Sandage, A. 1961, *The Hubble Atlas of Galaxies*, Carnegie Inst Washington Publ. No. 618
- Sandage, A. & Tammann, G. 1981, *A Revised Shapley-Ames Catalogue*, Carnegie Inst. Washington Publ. No. 635
- Schinnerer, E., Eckart, A., Quirrenbach, A., Boker, T., Tacconi-Garman, L. E., & Krabbe, A. 1997, *ApJ*, 488, 174
- Schwarz, M. P. 1981, *ApJ*, 247, 77
- Schwarz, M. P. 1984a, *MNRAS*, 209, 93
- Schwarz, M. P. 1984b, *Proc. Astron. Soc. Aust.*, 5, 464
- Schwarz, M. P. 1985, *Proc. Astron. Soc. Aust.*, 6, 202
- Schweizer, F., Ford, W. K., Jr., Jederzejewski, R., Giovanelli, & R. 1987, *ApJ*, 320, 454
- Schweizer, F., van Gorkom, J. H., & Seitzer, P. 1989, *ApJ*, 338, 770
- Seaton, M. J. 1979, *MNRAS*, 187, 73
- Sellwood, J. A. & Wilkinson, A. 1993, *Rep. Prog. Phys.* 56, 173
- Shen, J. & Sellwood, J. A. 2004, *ApJ*, 604, 614
- Sil'chenko, O. K. & Moiseev, A. V. 2006, *AJ*, 131, 1336
- Simkin, S. M., Su, H. J., & Schwarz, M. P. 1980, *ApJ*, 237, 404
- Struck, C. 2010, *MNRAS*, 403, 1516
- Tamburro, D., Rix, H.-W., Walter, F., Brinks, E., de Blok, W. J. G., Kennicutt, R. C., & MacLow, M.-M. 2008, *AJ*, 136, 2872
- Tomita, A., Tomita, Y., & Saito, M. 1996 *PASJ*, 48, 285
- Truthardt, P., Salo, H., Rautiainen, P., & Buta, R. J. 2008, *AJ*, 134, 1195
- Wozniak, H., Friedli, D., Martinet, L., Martin, P., & Bratschi, P. 1995, *A&AS*, 111, 115

Wu, W. 2008, *AJ*, 135, 268

Wu, W. 2009, *AJ*, 137, 3455

Yasuda, N., Fukugita, M., & Okamura, S. 1997, *ApJS*, 108, 417

Zhang, X. & Buta, R. J. 2007, *AJ*, 133, 258

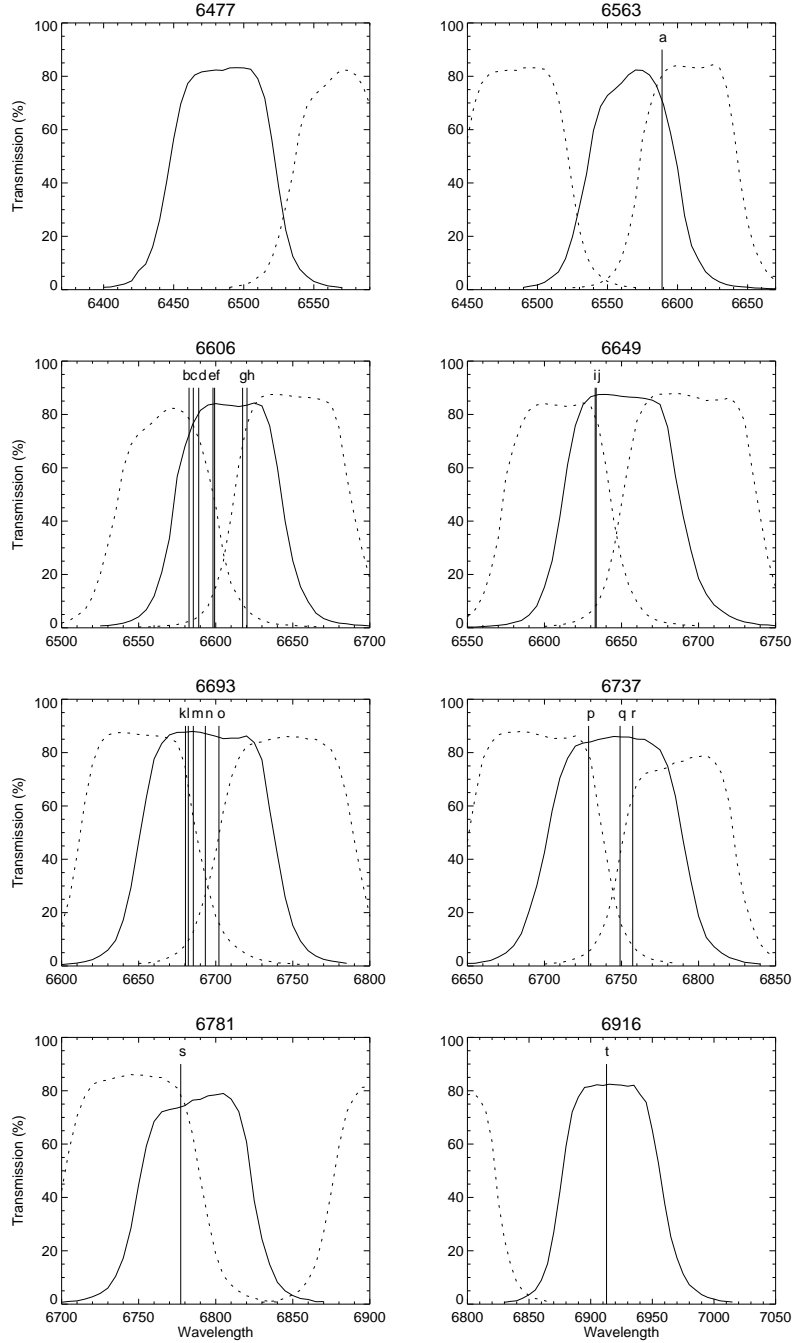


Fig. 1.— Transmission properties of the narrowband filters used to observe our sample. Each panel is centered on a filter (solid line) whose central wavelength in Angstroms is labeled above. Nearby filters (dashed lines) are included for comparison. For each galaxy, we included a vertical line representing the wavelength of its redshifted H α emission. The lines are labeled alphabetically and correspond to the sample in the following way: a) NGC 5530, b) NGC 7217, c) IC 1993, d) NGC 5364, e) NGC 7742, f) IC 5267, g) ESO 399-25, h) NGC 7187, i) NGC 7020, j) NGC 7702, k) ESO 286–10, l) ESO 198–13, m) ESO 234–11, n) ESO 526–7, o) ESO 297–27 p) ESO 231–1, q) ESO 409–3, r) ESO 576–57, s) ESO 111–22, and t) ESO 236–29

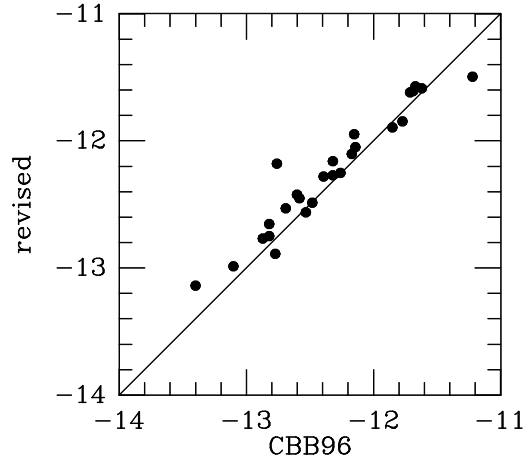


Fig. 2.— Comparison between H α + [NII] fluxes estimated for 30 galaxies by CBB96 and those estimated in the re-analysis. The solid line has a unit slope.

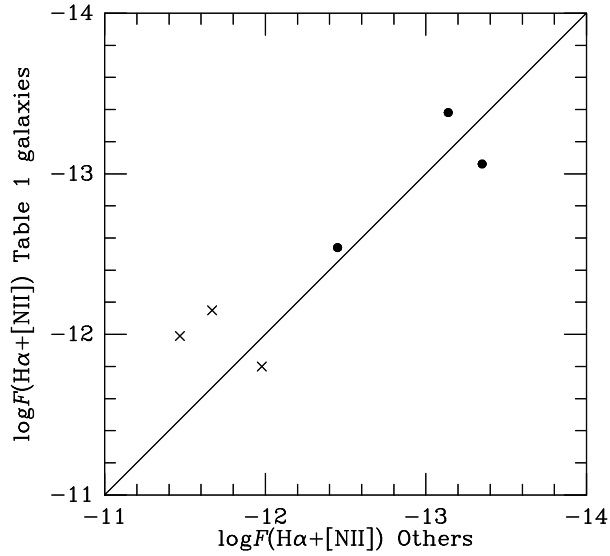


Fig. 3.— Comparison between H α + [NII] fluxes for six galaxies in Table 1 compared with values for the same galaxies from Kennicutt & Kent (1983, crosses: NGC 5364, 7217, and NGC 7742) and from Table 2 of this paper (filled circles: NGC 7020, NGC 7187, and NGC 7702). The solid line has a unit slope.

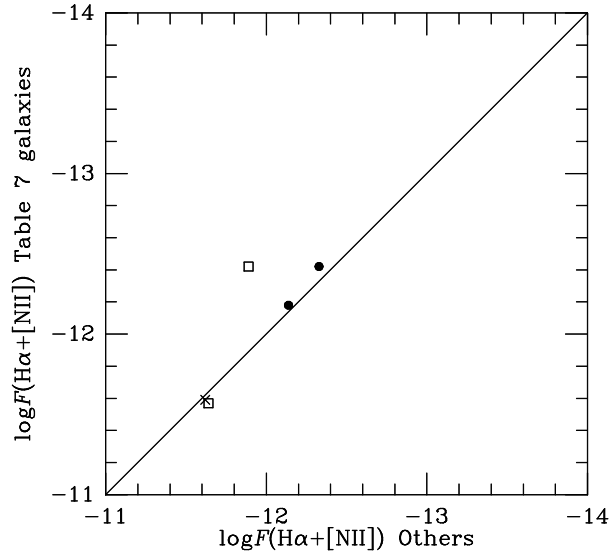


Fig. 4.— Comparison between $\text{H}\alpha + [\text{NII}]$ fluxes for three galaxies in Table 2 compared with values for the same galaxies from Kennicutt & Kent (1983, crosses: NGC 1832), Hameed & Devereux (1999, open squares: NGC 1350 and NGC 1433), and Koopmann & Kenney (2006, filled circles: IC 5240 and NGC 7098). The solid line has a unit slope.

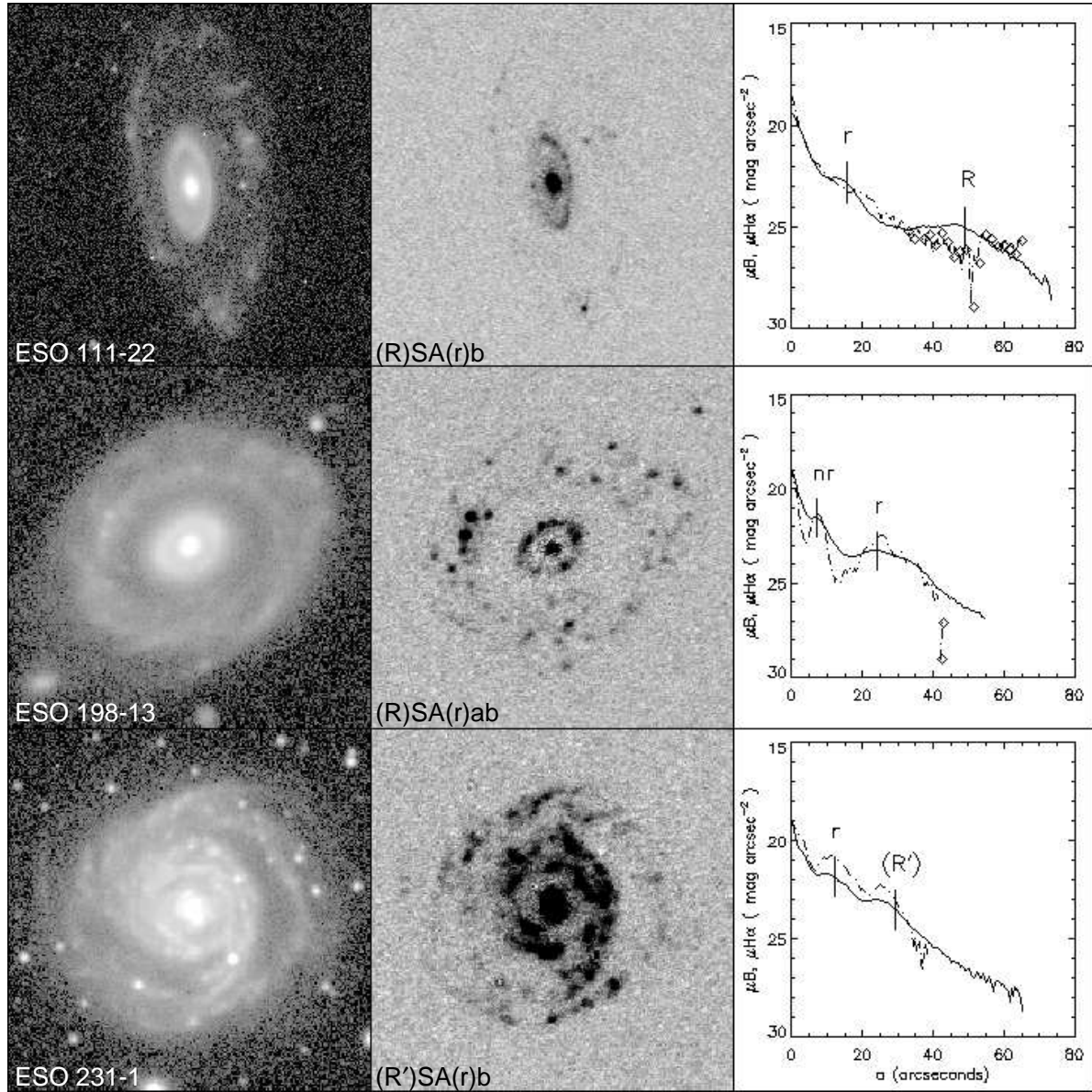


Fig. 5.— B -band (left column) and $H\alpha$ (middle column) images, and B -band (solid line) and $H\alpha$ (dashed line) surface brightness profiles (right column) of ESO 111–22 (top row), ESO 198–13 (middle row), and ESO 231–1 (bottom row). The ESO 198–13 and ESO 231–1 images have a width of $1''.5$. The ESO 111–22 images are $2''.2$ across. The vertical lines on the surface brightness profiles indicate the semimajor axis of the rings (see Table 7). For ESO 198–13, the outer ring was not detected in the $H\alpha$ image and is not, therefore, labeled. The diamonds on the $H\alpha$ profile indicate the radii at which the azimuthally averaged flux drops below the uncertainty in the sky. Each image is oriented with north up and east to the left.

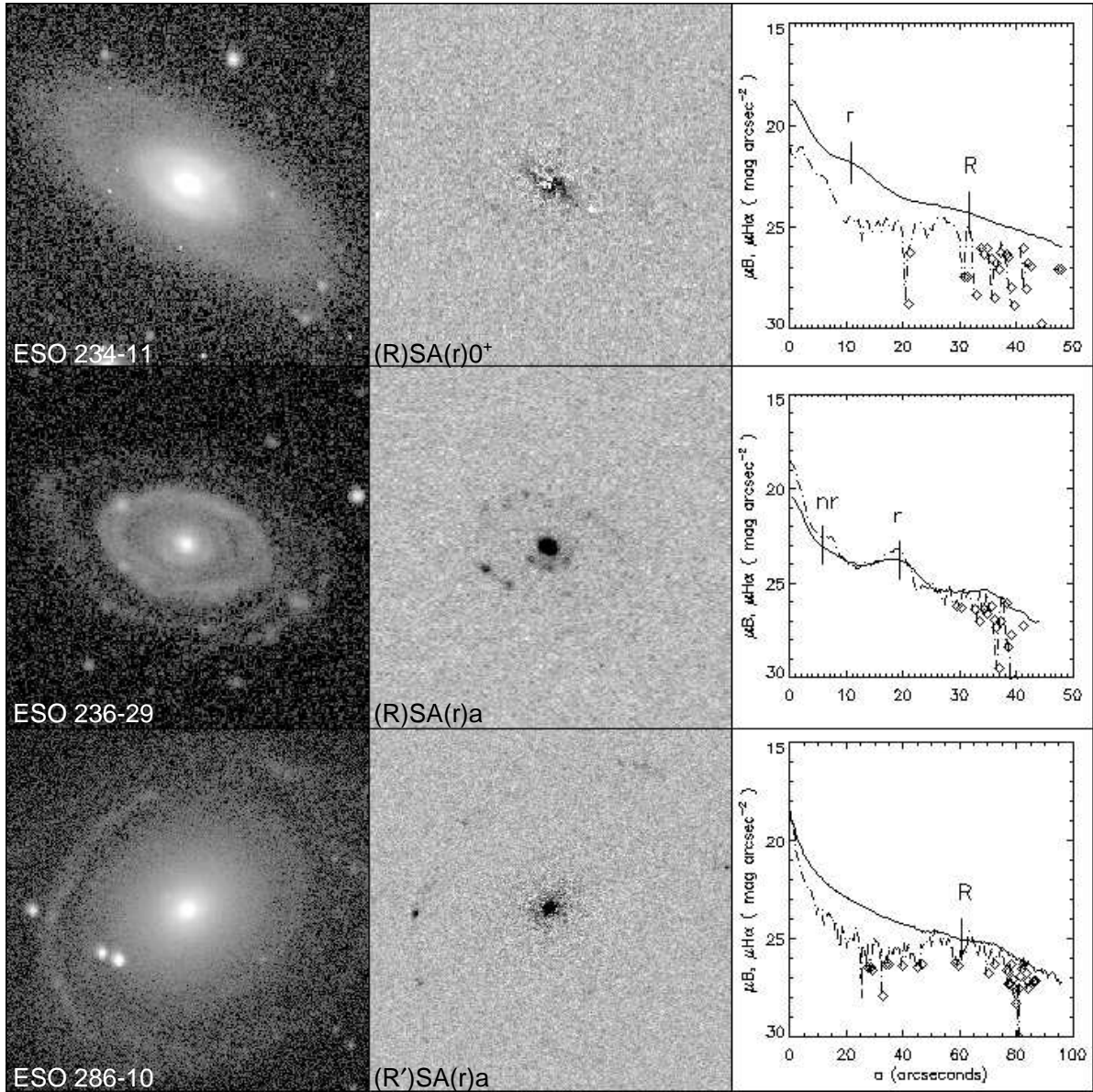


Fig. 6.— B -band (left column) and $H\alpha$ (middle column) images, and B -band (solid line) and $H\alpha$ (dashed line) surface brightness profiles (right column) of ESO 234–11 (top row), ESO 236–29 (middle row), and ESO 286–10 (bottom row). The ESO 234–11 and ESO 236–29 images have a width of $1''.5$. The ESO 286–10 images are $2''.2$ across. The vertical lines on the surface brightness profiles indicate the semimajor axis of each ring (see Table 7). For ESO 234–11, the ring sizes are based on the broadband image since neither ring was detected in $H\alpha$. For ESO 236–29, we were able to detect the nuclear and inner rings, but not the outer ring in $H\alpha$. For ESO 286–10, we were able to detect the outer ring, but not the inner ring in $H\alpha$. The diamonds on the $H\alpha$ profile indicate the radii at which the azimuthally averaged flux drops below the uncertainty in the sky. Each image is oriented with north up and east to the left.

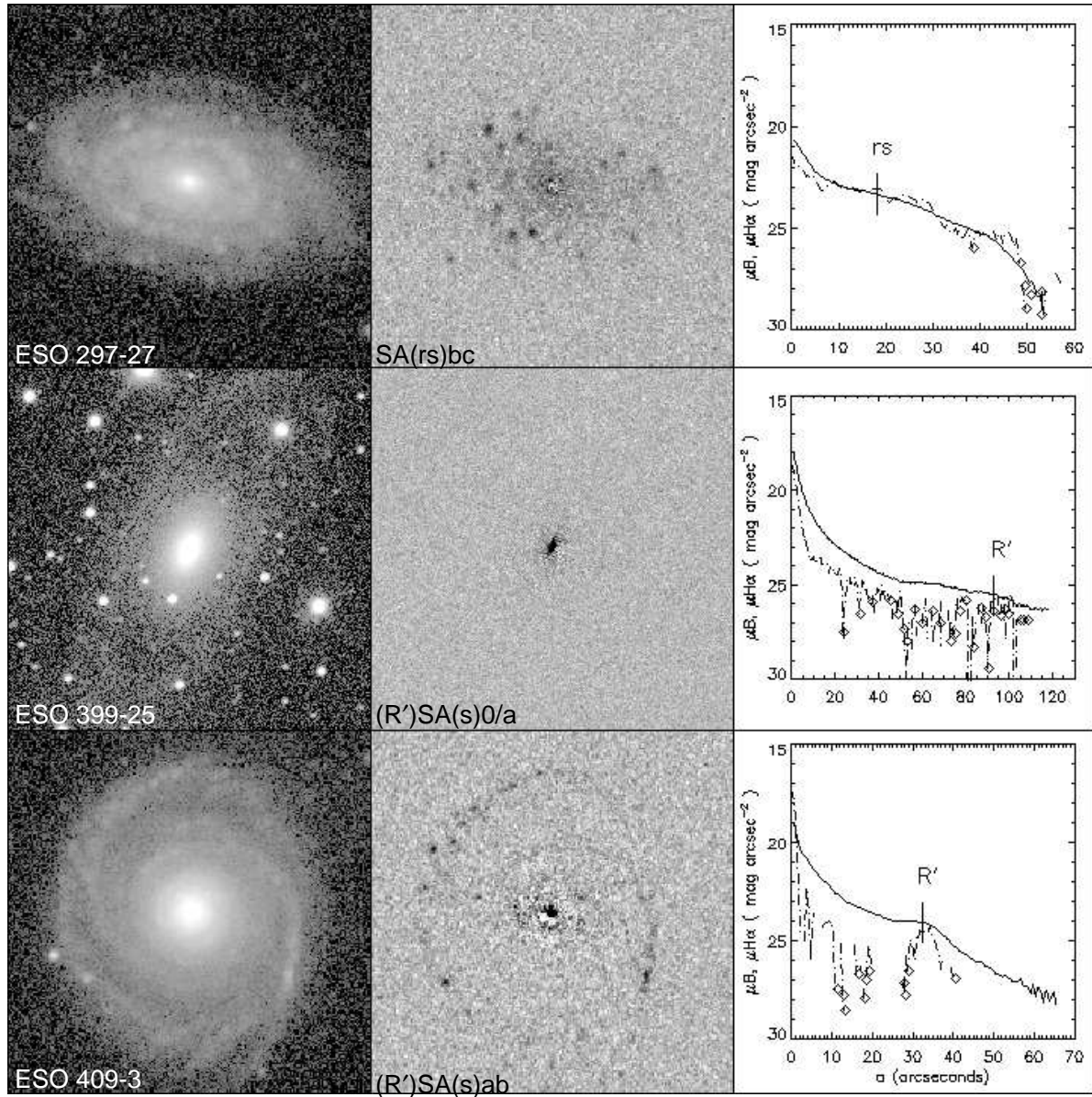


Fig. 7.— B -band (left column) and $H\alpha$ (middle column) images, and B -band (solid line) and $H\alpha$ (dashed line) surface brightness profiles (right column) of ESO 297–27 (top row), ESO 399–25 (middle row), and ESO 409–3 (bottom row). The ESO 297–27 and ESO 409–3 images are $1.5''$ across. The ESO 399–25 images are $2.9''$ across. The vertical lines on the surface brightness profiles indicate the ring’s semimajor axis (see Table 7). For ESO 399–25, the size of the pseudoring is based on the broadband image since the ring was not detected in $H\alpha$. The diamonds on the $H\alpha$ profile indicate the radii at which the azimuthally averaged flux drops below the uncertainty in the sky. Each image is oriented with north up and east to the left.

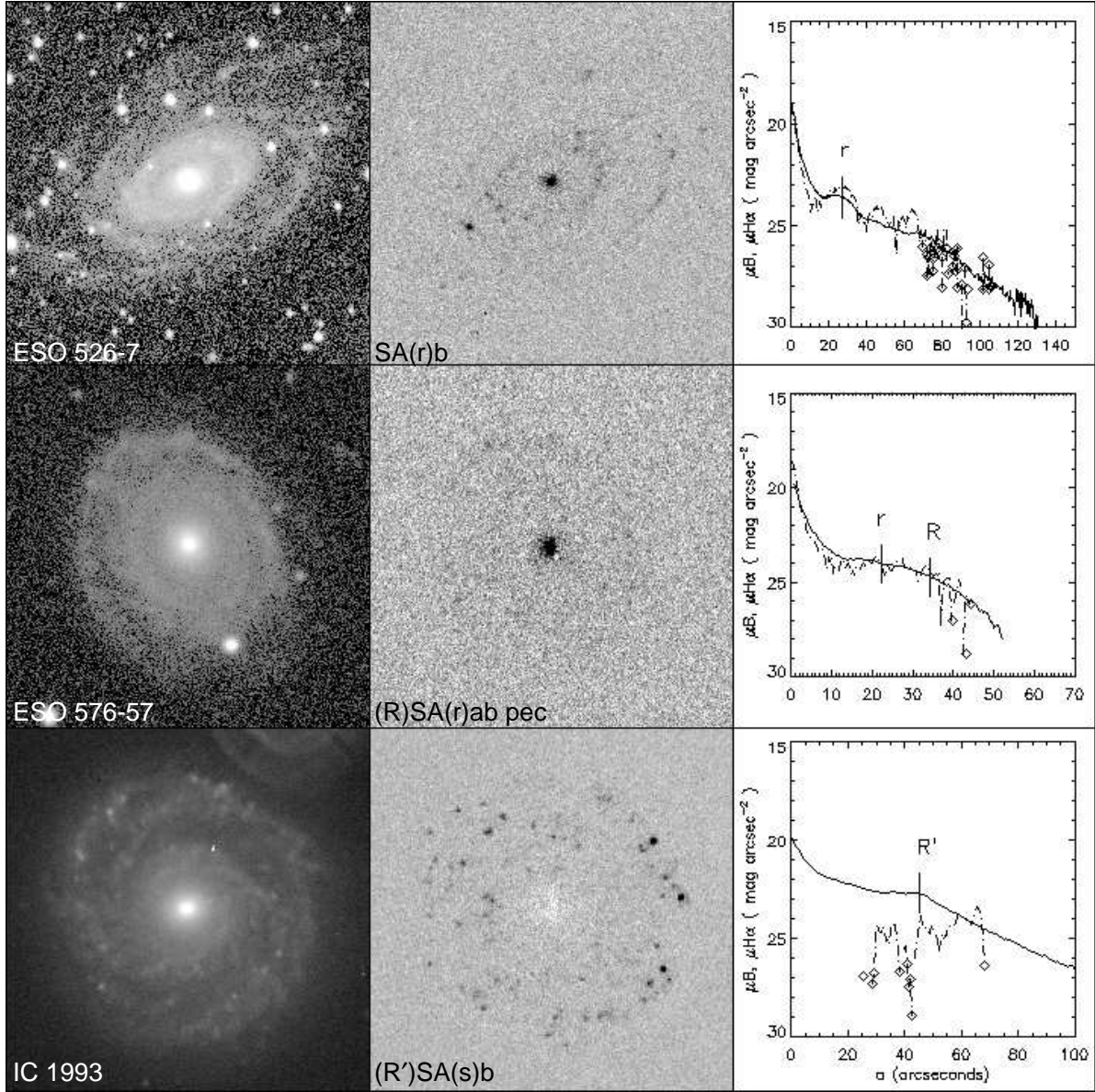


Fig. 8.— B -band (left column) and $H\alpha$ (middle column) images, and B -band (solid line) and $H\alpha$ (dashed line) surface brightness profiles (right column) of ESO 526–7 (top row), ESO 576–57 (middle row), and IC 1993 (bottom row). The ESO 526–7 images have a scale of $2''.9$, and the ESO 576–57 images have a scale of $1''.8$. The IC 1993 images have a scale of $2''.2$. The vertical lines on the surface brightness profiles indicate the ring’s semimajor axis (see Table 7). The diamonds on the $H\alpha$ profile indicate the radii at which the azimuthally averaged flux drops below the uncertainty in the sky. Each image is oriented with north up and east to the left.

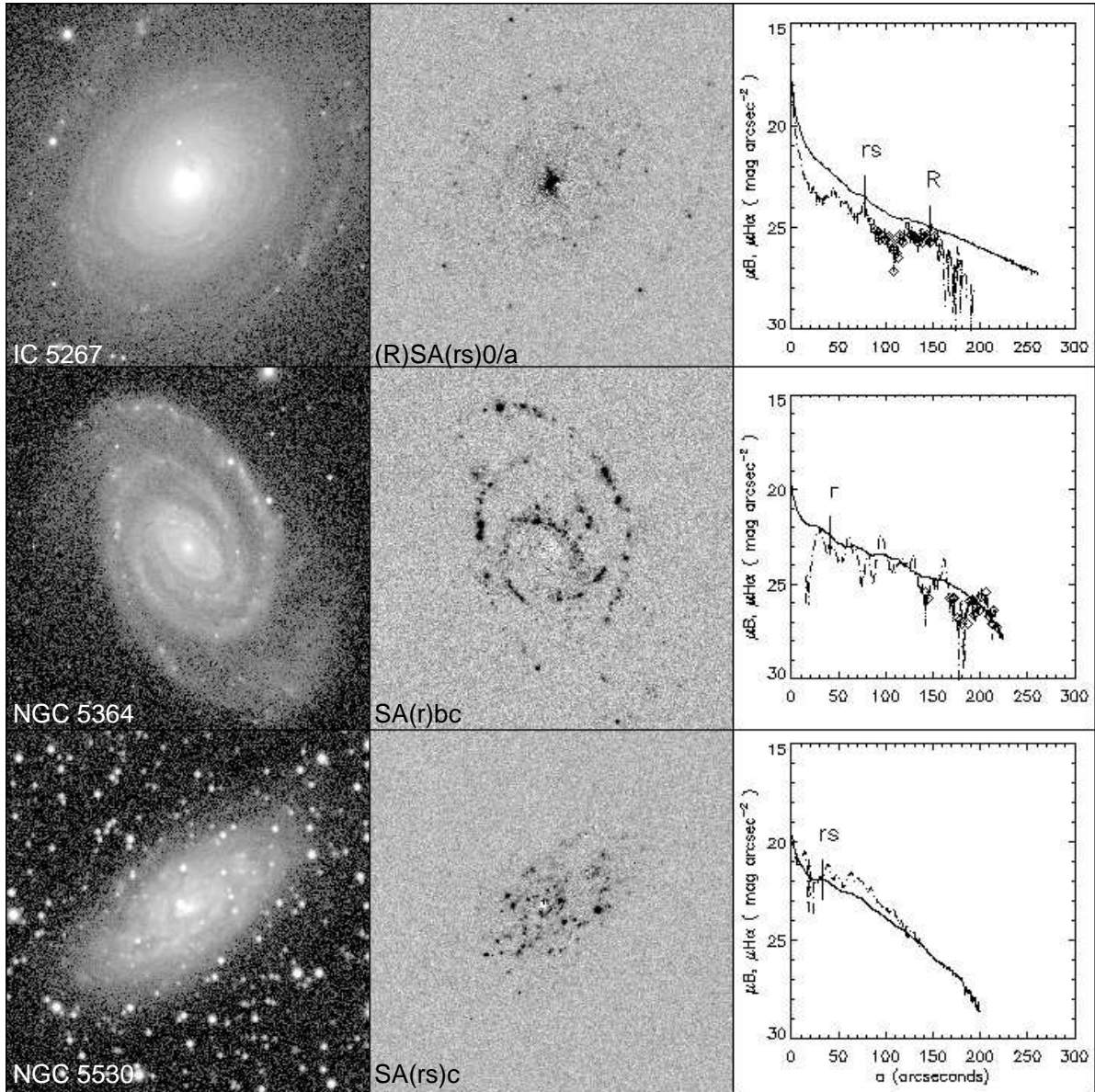


Fig. 9.— B -band (left column) and $H\alpha$ (middle column) images, and B -band (solid line) and $H\alpha$ (dashed line) surface brightness profiles (right column) of IC 5267 (top row), NGC 5364 (middle row), and NGC 5530 (bottom row). The IC 5267 images have a scale of $4''.3$. The NGC 5364 images have a scale of $6''.5$. The NGC 5530 images have a scale of $5''.8$. The vertical lines on the surface brightness profiles indicate the ring’s semimajor axis (see Table 7). The diamonds on the $H\alpha$ profile indicate the radii at which the azimuthally averaged flux drops below the uncertainty in the sky. Each image is oriented with north up and east to the left.

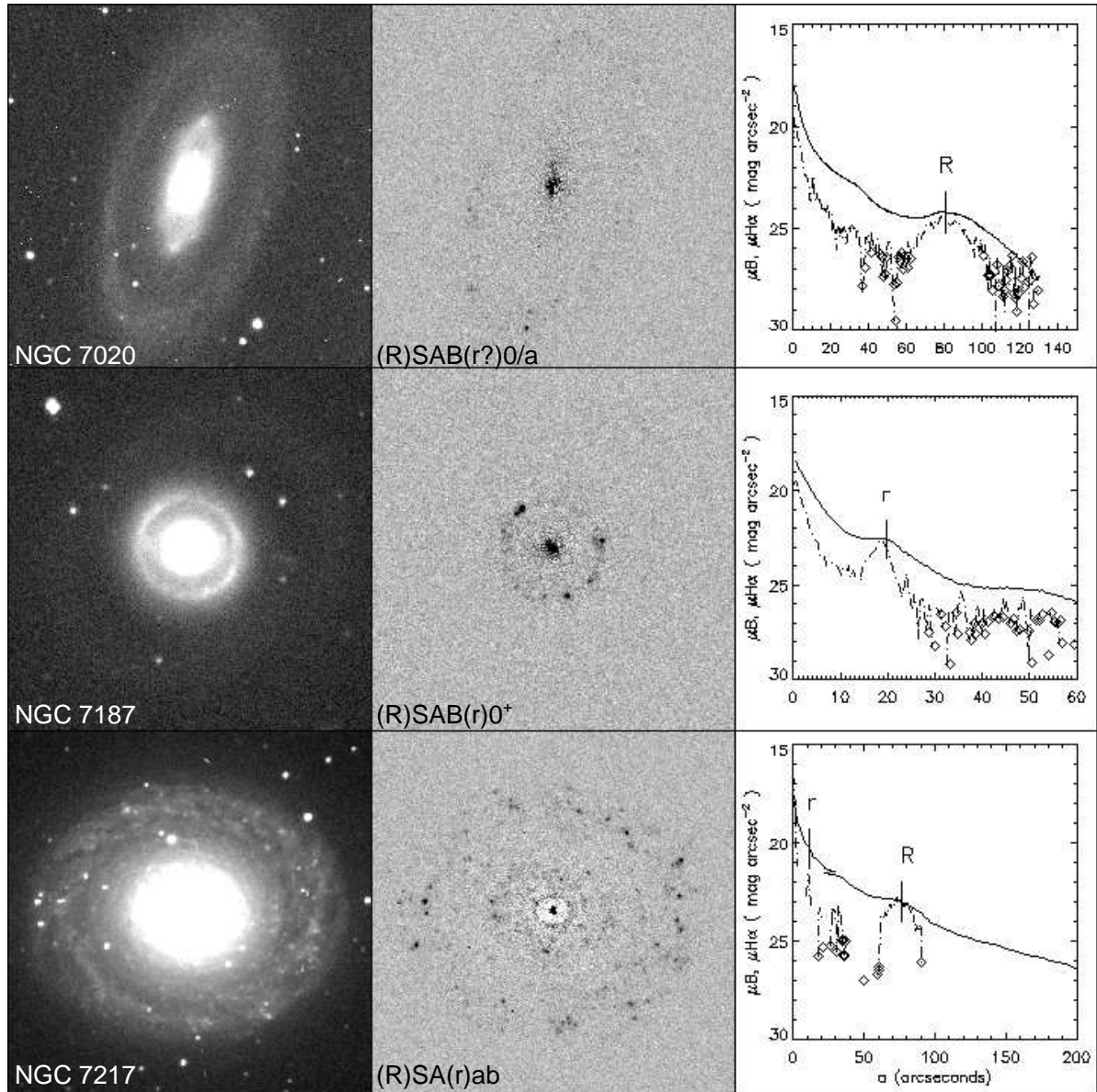


Fig. 10.— B -band (left column) and $H\alpha$ (middle column) images, and B -band (solid line) and $H\alpha$ (dashed line) surface brightness profiles (right column) of NGC 7020 (top row), NGC 7187 (middle row), and NGC 7217 (bottom row). The NGC 7020 images have a scale of $3''.3$. The NGC 7187 images have a scale of $2''.2$. The NGC 7217 images have a scale of $3''.5$. The vertical lines on the surface brightness profiles indicate the ring's semimajor axis (see Table 7). For NGC 7020, the outer ring was faintly detectable, but the inner ring was not detected in $H\alpha$. For NGC 7187, the inner ring was present while the outer ring was not detected in $H\alpha$. The diamonds on the $H\alpha$ profile indicate the radii at which the azimuthally averaged flux drops below the uncertainty in the sky. Each image is oriented with north up and east to the left.

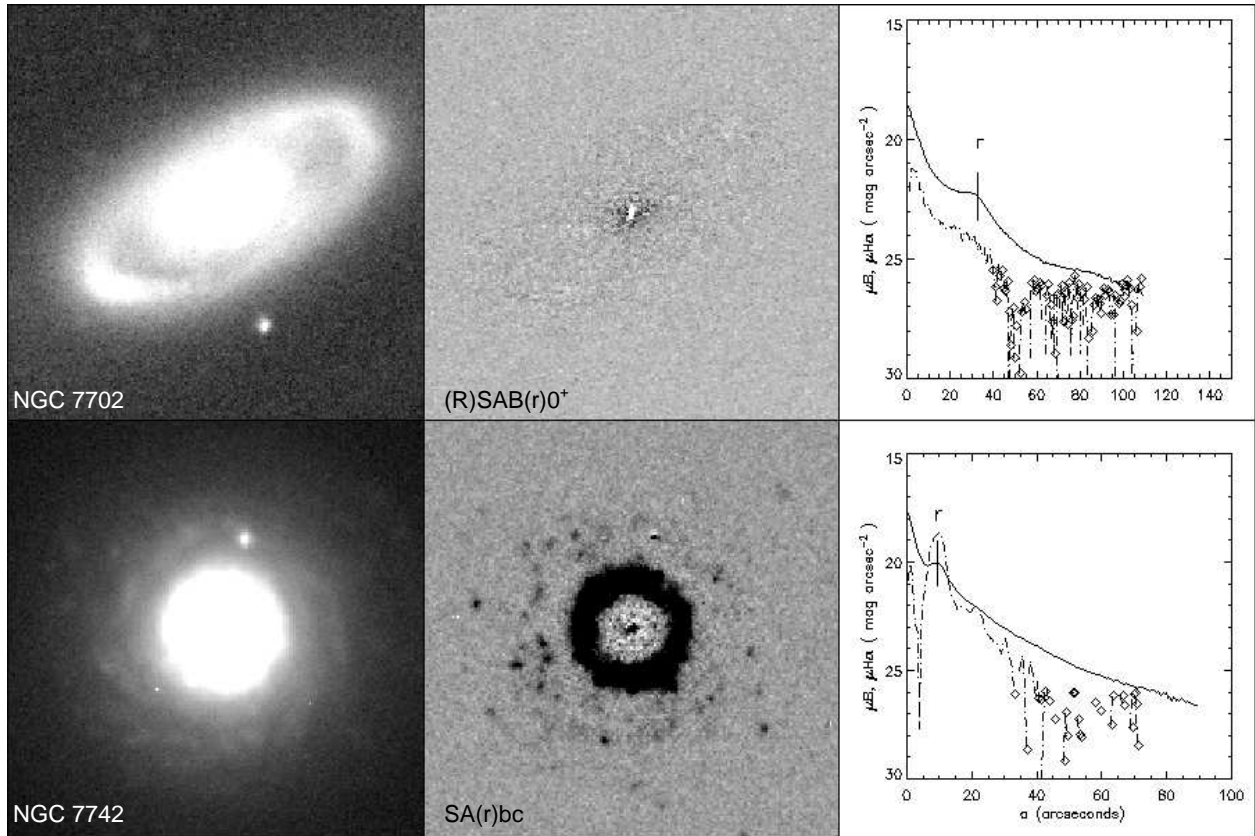


Fig. 11.— B -band (left column) and $H\alpha$ (middle column) images, and B -band (solid line) and $H\alpha$ (dashed line) surface brightness profiles (right column) of NGC 7702 (top row) and NGC 7742 (bottom row). The NGC 7702 images a scale of $1.''5$, and the NGC 7742 images have a scale of $1.''3$. The vertical lines on the surface brightness profiles indicate the ring’s semimajor axis (see Table 7). For NGC 7702, the size of the inner ring is based on the broadband image of the galaxy since neither ring was detected in $H\alpha$. It should also be noted that the faint outer ring of NGC 7702 is not shown in the B -band image. The diamonds on the $H\alpha$ profile indicate the radii at which the azimuthally averaged flux drops below the uncertainty in the sky. Each image is oriented with north up and east to the left.

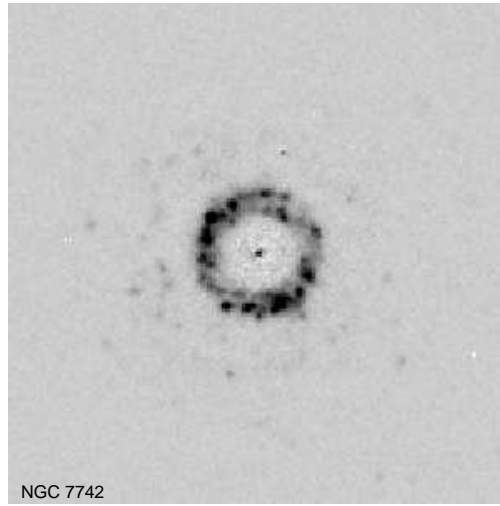


Fig. 12.— Close up of NGC 7742 showing the braided morphology of the inner ring. It appears to be made up of two spiral arms wound around each other. The panel is $1''.45$ wide, and the image is oriented with north up and east to the left.

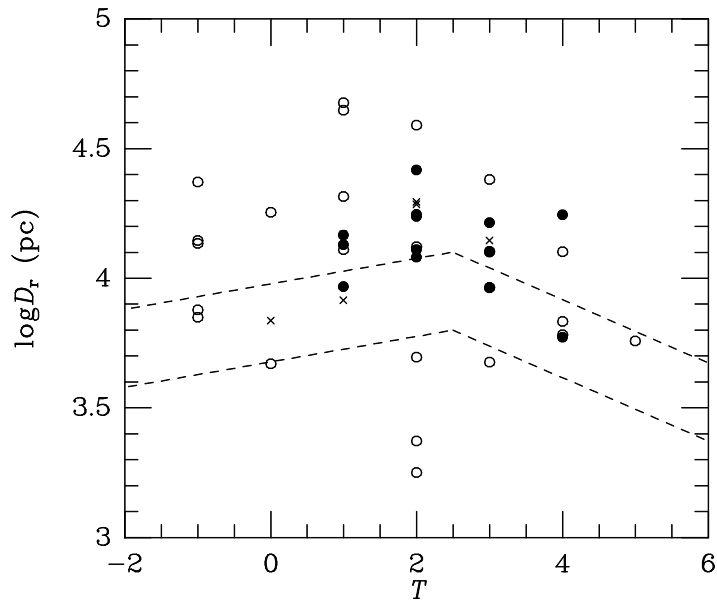


Fig. 13.— Plot of the log of the deprojected inner ring diameter vs. de Vaucouleurs type index. The dashed lines are for SB galaxies (upper) and SA galaxies (lower) as derived for a nearby galaxy sample by Buta & de Vaucouleurs (1982), adjusted for Hubble constant. The points plotted are for the combined barred/nonbarred galaxy sample, with filled circles for SB types, crosses for SAB types, and open circles for SA types.

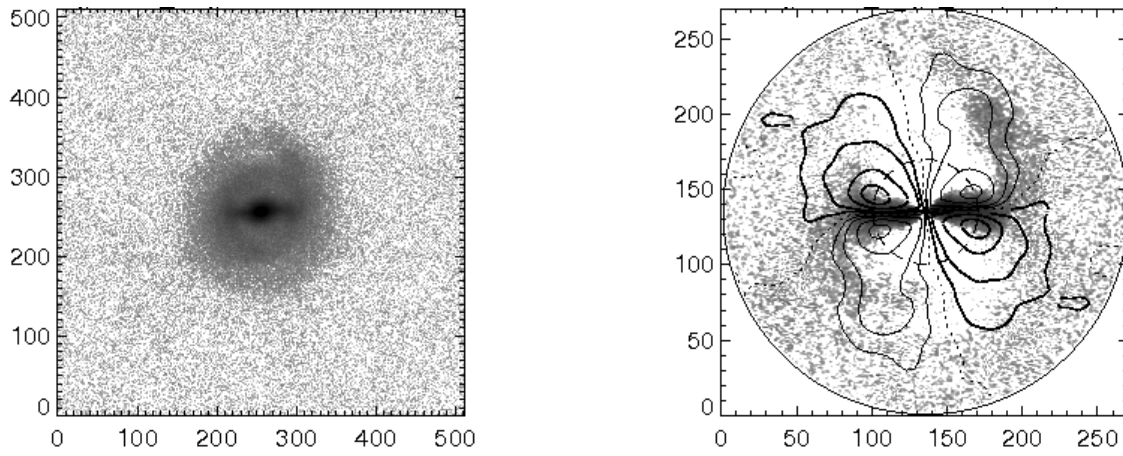


Fig. 14.— Example images associated with measuring the bar strength for the barred galaxy NGC 6761 from the CBB96 data. Left: the red continuum image of the galaxy used to estimate the galaxy’s potential. Right: the force ratio map overlaid onto the red continuum image minus $m = 0$ Fourier component.

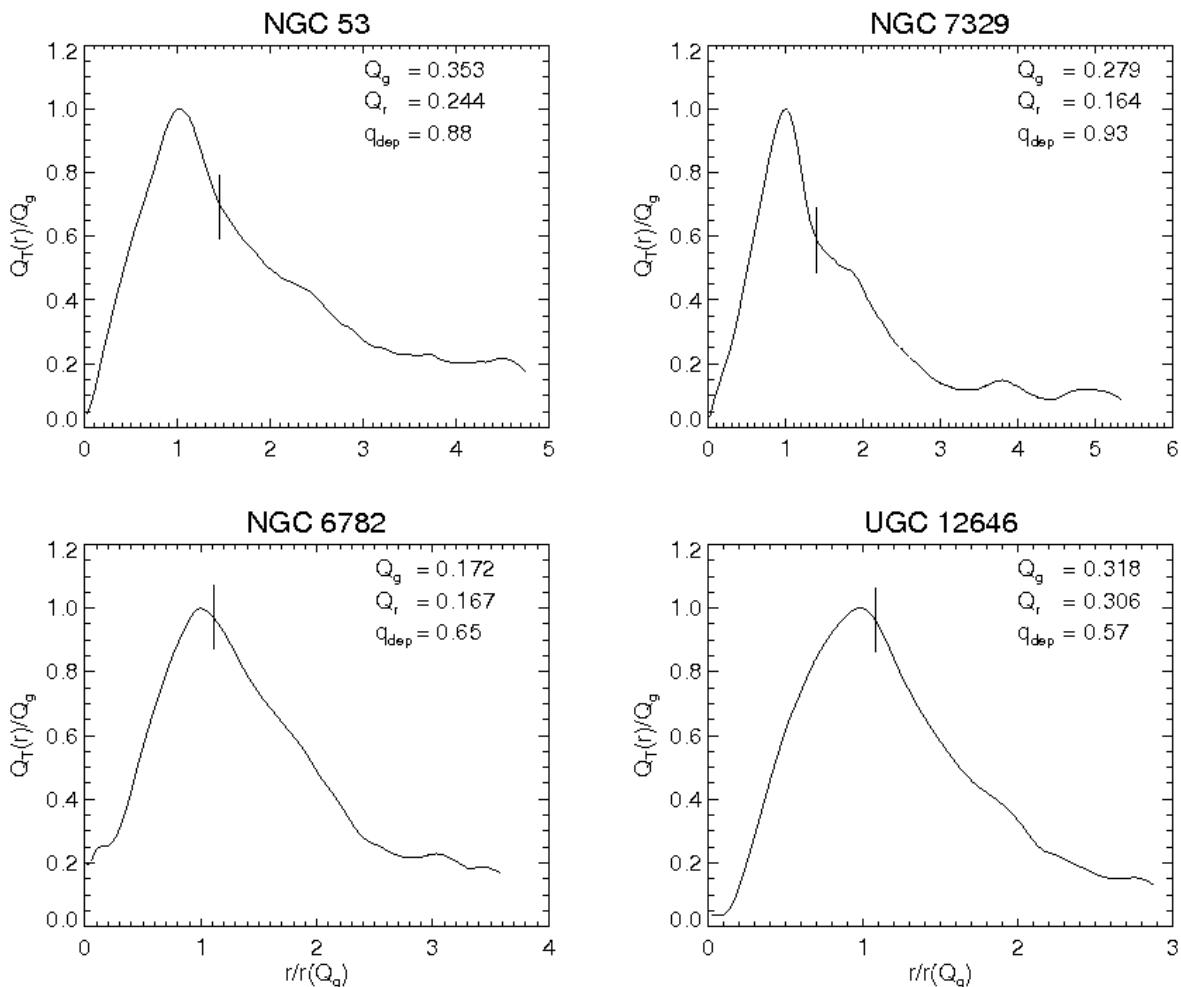


Fig. 15.— Plot demonstrating the relationship between Q_g , Q_b , and Q_r as defined for this study. Each panel shows the strength of the non-axisymmetric perturbation as a function of radius for a strongly barred galaxy: NGC 53 (upper left), NGC 7329 (upper right), NGC 6782 (lower left), and UGC 12646 (lower right). Each galaxy has a number associated with it which represents the maximum value in this profile. We call this maximum value Q_g . If Q_g occurs in the region of the bar, as it does for each of these galaxies, then Q_g becomes Q_b and is a measure of bar strength. For each galaxy the value of Q_g is listed in the upper right-hand corner of the panel. Also for each galaxy, we have placed a line representing the position of the ring. The measure of the non-axisymmetric perturbation in the location of the ring is called Q_r . For NGC 6782 and UGC 12646, the position of the ring is very close to the position where Q_g is measured. For NGC 53 and NGC 7329, the ring position is outside of the bar region.

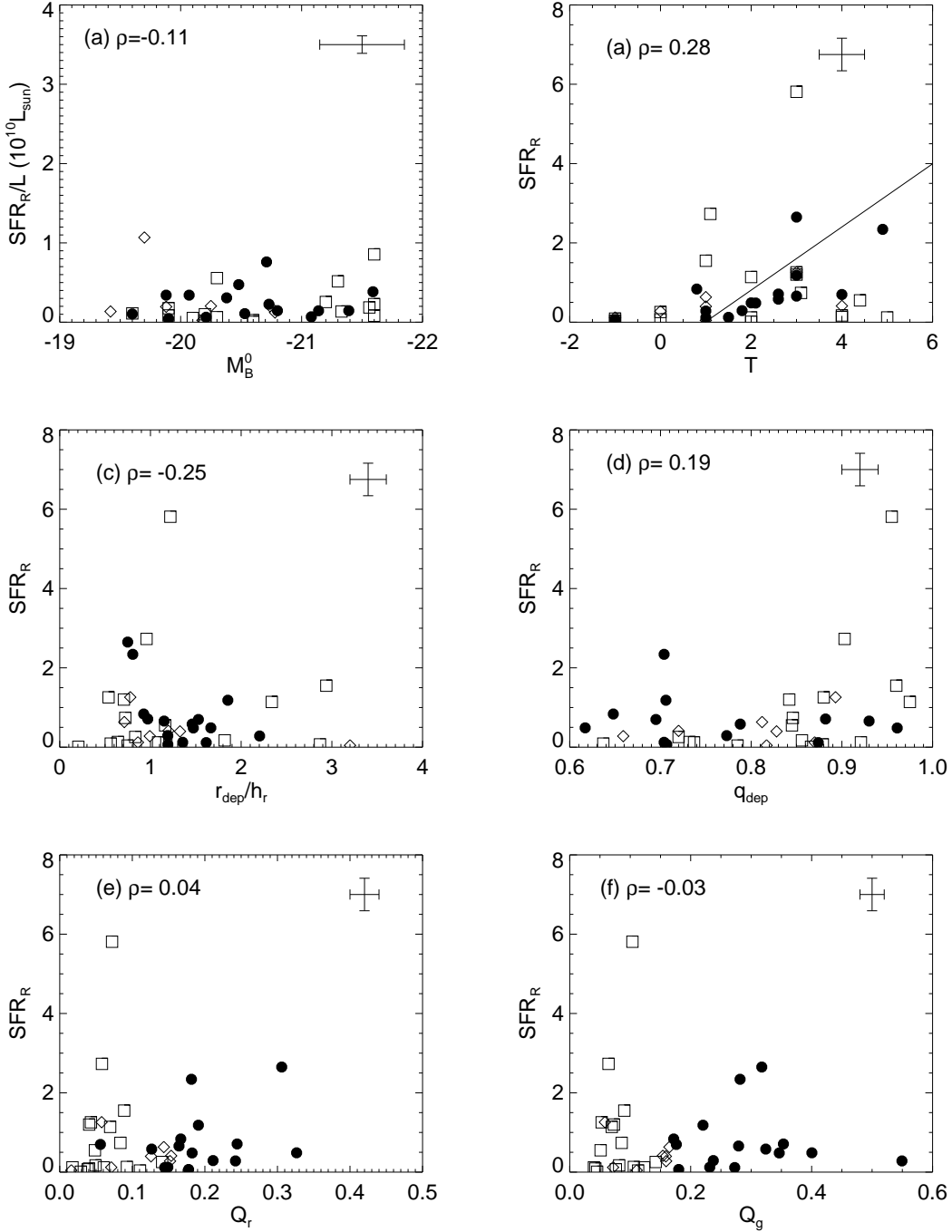


Fig. 16.— Plots of inner ring SFR in units of solar masses per year vs. (a) the absolute blue magnitude of the parent galaxy; (b) the de Vaucouleurs type of the parent galaxy; (c) the ratio of the deprojected radius of the main ring to the radial scale length of the parent galaxy, which is unitless; (d) the deprojected axis ratio of the inner ring in arcseconds; (e) Q_r ; and (f) Q_g . For all panels, the open squares refer to SA galaxies, open diamonds refer to SAB galaxies, and solid points refer to SB galaxies. In the upper left-hand corner of each panel is a representative errorbar of median parameters. The OLS bisector line is included in the plots in which the correlation was found to be significant as discussed in the text.

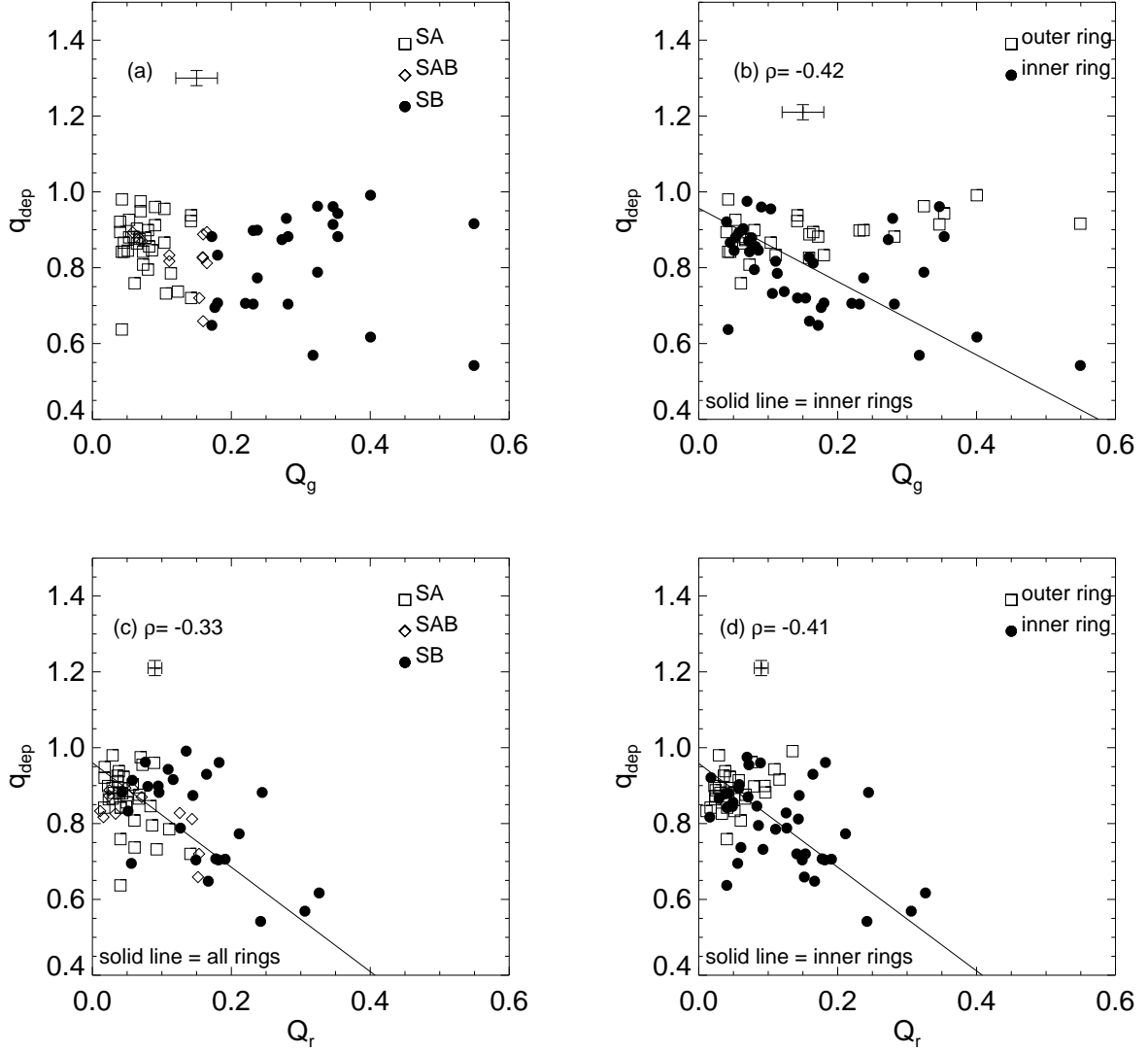


Fig. 17.— Deprojected ring shape vs. (a) and (b) Q_g , and (c) and (d) Q_r . The shape of the outer ring is not correlated to Q_g or Q_r . However, inner rings are related to Q_g and Q_r . For plots (a) and (c) open squares refer to SA galaxies, open diamonds refer to SAB galaxies, and solid points refer to SB galaxies. For plots (b) and (d) open squares refer to outer rings, and solid points refer to inner rings. The OLS bisector line is included in the plots in which the correlation was found to be significant as discussed in the text with the corresponding rank correlation coefficient displayed in the upper left corner.

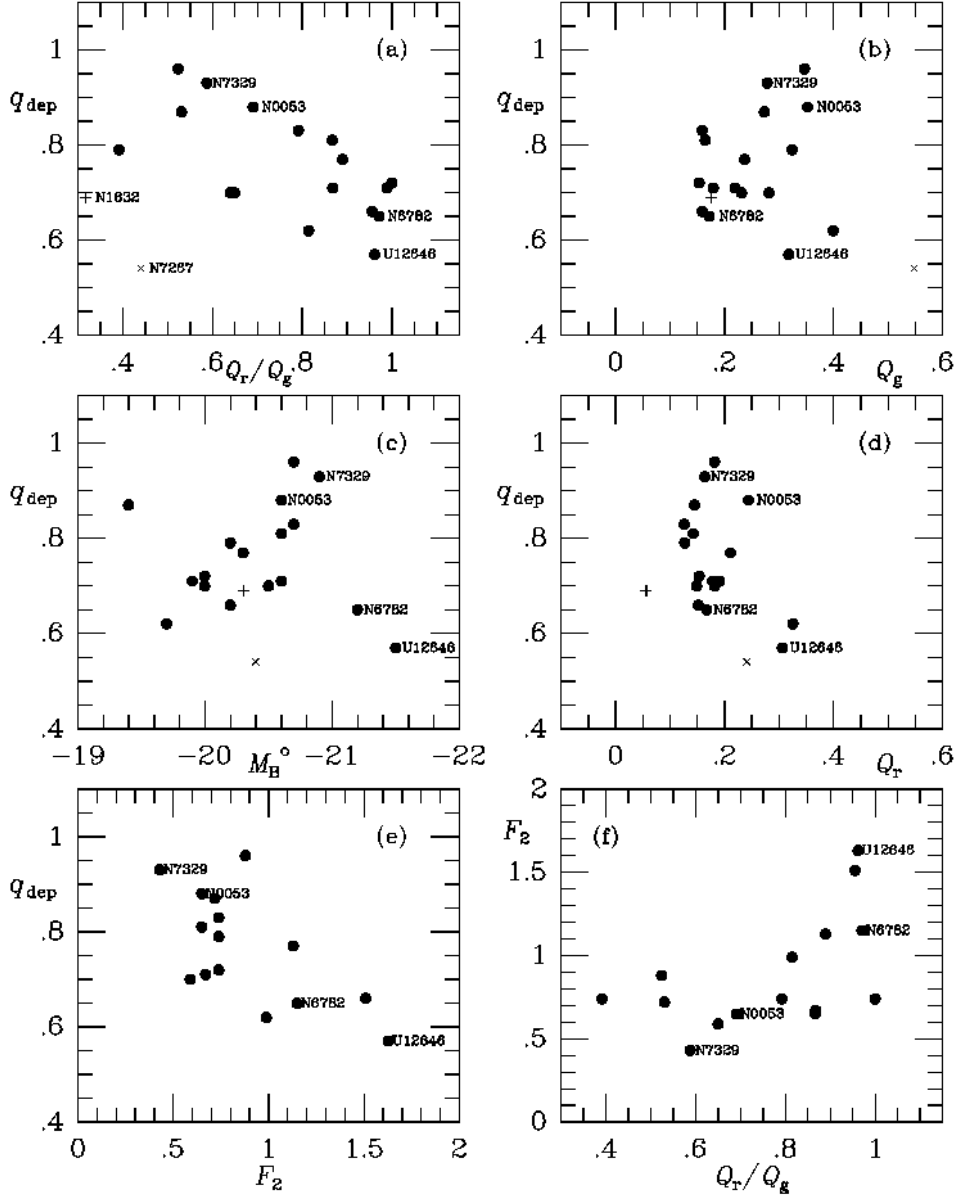


Fig. 18.— Plots of 15 CBB96 galaxies having $Q_g \geq 0.15$. Constraining Q_g in this way ensures that barred galaxies are selected. The first five panels show the deprojected ring shape (q_{dep}) vs. (a) the relative forcing parameter (Q_r/Q_g), (b) Q_g , (c) absolute blue magnitude M_B^o , (d) Q_r , and (e) the relative amplitude of the H α flux around the ring, F_2 . Panel (f) shows F_2 vs. Q_r/Q_g .

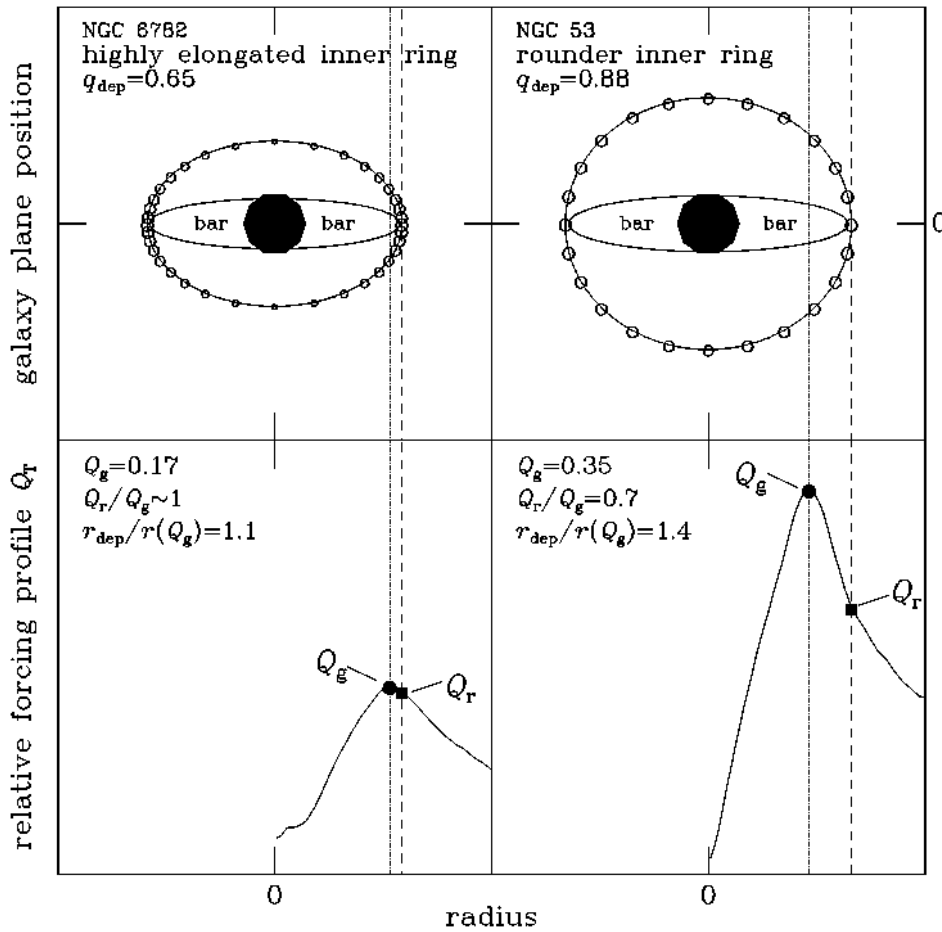


Fig. 19.— Schematics of the deprojected inner rings of NGC 6782 and NGC 53 to highlight how the shape of the ring may be tied to the relative forcing parameter Q_r/Q_g , rather than to just Q_g or Q_r . NGC 53 has a rounder inner ring than does NGC 6782, even though Q_r for NGC 53 exceeds Q_g for NGC 6782. The small open circles lining the inner rings are intended to highlight how the distribution and even luminosities of HII regions vary around the rings in a manner dependent on the inner ring axis ratio.

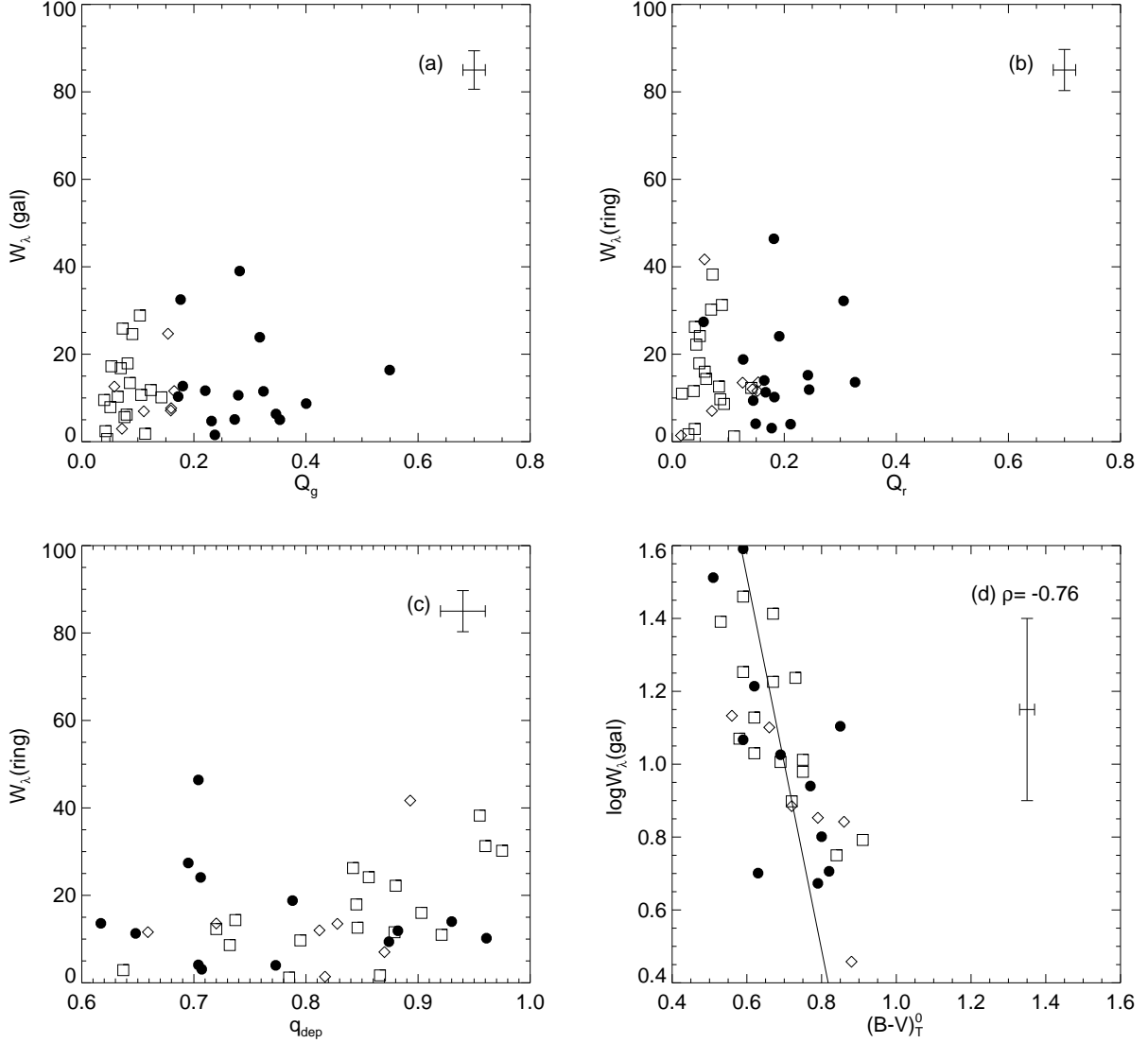


Fig. 20.— Plots of (a) the global galaxy equivalent width of $H\alpha+[NII]$ emission vs. Q_g ; (b) the equivalent width of inner ring $H\alpha+[NII]$ emission vs. Q_r ; (c) the equivalent width of inner ring $H\alpha+[NII]$ emission vs. the inner ring’s deprojected axis ratio; (d) the log of the global equivalent width of $H\alpha+[NII]$ vs. the corrected total color index, following Kennicutt (1983). In each plot, open squares refer to SA galaxies, open diamonds refer to SAB galaxies, and solid points refer to SB galaxies. In the upper right hand corner of each panel is a representative errorbar based on median parameters. The OLS bisector line and the Spearman rank coefficient are included in the plots in which the correlation was found to be significant as discussed in the text.

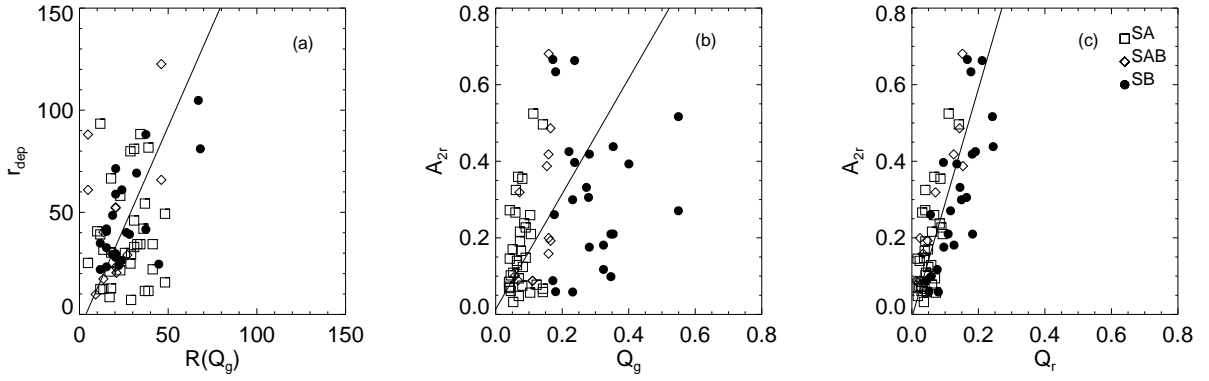


Fig. 21.— Plots of (a) the semimajor axis of the deprojected ring, in arcseconds, vs. the location of Q_g ; (b) the $m = 2$ Fourier amplitude at the location of the ring vs. Q_g ; and (c) the $m = 2$ Fourier amplitude at the position of the ring vs. Q_r . The OLS bisector line is included in the plots in which the correlation was found to be significant as discussed in the text.

Table 1. Basic Parameters of Observed Galaxies^a

Name	Type	Type Source	B_T^0	V_{sun} (km s ⁻¹)	Distance (Mpc)
ESO 111-22	(R)SA(r)b	deVA	14.38 ± 0.15	9796 ± 26	133.0 ± 9.3
ESO 198-13	(R)SA(r)ab	deVA	14.02 ± 0.21	5452 ± 27	73.1 ± 5.1
ESO 231-1	(R')SA(r)b	CSRG	13.46 ± 0.16	7575 ± 13	103.1 ± 7.2
ESO 234-11	(R)SA(r)0 ⁺	CSRG	14.35 ± 0.04	5604 ± 26	76.4 ± 5.4
ESO 236-29	(R)SA(r)a	deVA	15.12 ± 1.05	15990 ± 52	218.6 ± 15.3
ESO 286-10	(R')SA(r)a	deVA	13.07 ± 0.11	5368 ± 25	73.4 ± 5.2
ESO 297-27	SA(<u>rs</u>)bc	GBSLS	14.51 ± 0.03	6362 ± 10	86.1 ± 6.0
ESO 399-25	(R')SA(s)0/a	CSRG	12.92 ± 0.06	2542 ± 6	35.1 ± 2.5
ESO 409-3	(R')SA(s)ab	CSRG	14.00 ± 0.13	8507 ± 15	116.7 ± 8.2
ESO 526-7	SA(r)b	deVA	12.98 ± 0.07	5959 ± 3	82.4 ± 5.8
ESO 576-57	(R)SA(r)ab p	CSRG	14.32 ± 0.11	4627 ± 10^b	61.7 ± 4.3
IC 1993	(R')SA(s)b	deVA	12.43 ± 0.14	1080 ± 3	13.1 ± 0.9
IC 5267	(R)SA(rs)0/a	CSRG	11.20 ± 0.02	1712 ± 4	23.2 ± 1.6
NGC 5364	SA(r)bc	deVA	10.81 ± 0.09	1241 ± 4	16.7 ± 1.2
NGC 5530	SA(<u>rs</u>)c	CSRG	10.91 ± 0.01	1193 ± 2	14.5 ± 1.0
NGC 7020	(R)SAB(r?)0/a	deVA	12.88 ± 0.13	3201 ± 26	42.7 ± 3.0
NGC 7187	(R)S <u>A</u> B(r)0 ⁺	deVA	13.46 ± 0.16	2670 ± 21	37.0 ± 2.6
NGC 7217	(R)SA(r)ab	deVA	10.47 ± 0.13	952 ± 2	16.0 ± 1.1
NGC 7702	(R)S <u>A</u> B(r)0 ⁺	CSRG	12.98 ± 0.06	3231 ± 24	43.2 ± 3.0
NGC 7742	S <u>A</u> B(r)ab	deVA	12.30 ± 0.05	1663 ± 1	24.8 ± 1.7

^aColumn 1: galaxy name; Column 2: galaxy classification; Column 3: source of galaxy classification where deVA is from the de Vaucouleurs Atlas of Galaxies (Buta et al. 2007) and CSRG is from the Catalogue of Southern Ringed Galaxies (Buta 1995); Column 4: the corrected total apparent magnitude of the galaxy; Column 5: the recessional velocity; Column 6: the galactocentric distance from NASA Extragalactic Database (NED).

^bThis is the current value listed on NED; however, when we observed the galaxy in 2002, the listed recessional velocity was 8883 ± 53 km s⁻¹.

Table 2. Basic Parameters of CBB96 Sample^a

Name	Type	Type Source	B_T^0	V_{sun} (km s ⁻¹)	Distance (Mpc)
NGC 53	(R')SB(r)ab	CSRG	13.20	4568 ± 26	61.2 ± 4.3
NGC 1317	(R')SAB(rl)0/a	CSRG	11.81	1941 ± 14	25.0 ± 1.8
NGC 1326	(R ₁)SB(rl)0/a	CSRG	11.25	1360 ± 1	17.0 ± 1.2
NGC 1350	(R' ₁)SB(r)ab	CSRG	10.87	1905 ± 3	24.5 ± 1.7
NGC 1433	(R' ₁)SB(rs)ab	CSRG	10.64	1075 ± 3	12.7 ± 0.9
NGC 1832	SB(r)bc	RC3	11.59	1939 ± 5	24.8 ± 1.7
NGC 6300	SB(rs)b	CSRG	10.20	1109 ± 3	13.7 ± 1.0
NGC 6753	(R')SA(r)b	CSRG	11.58	3169 ± 8	42.5 ± 3.0
NGC 6761	(R')SB(r)0/a	CSRG	13.63	5650 ± 51	76.8 ± 5.4
NGC 6782	(R' ₁)SB(r)0/a	CSRG	12.21	3920 ± 14	52.6 ± 3.7
NGC 6902	SA(r)b	CSRG	11.58	2796 ± 4	38.2 ± 2.7
NGC 6935	(R)SA(r)a	CSRG	12.65	4543 ± 18	61.7 ± 4.3
NGC 6937	(R')SB(r)c	CSRG	13.35	4777 ± 6	64.9 ± 4.5
NGC 7020 ^b	(R)SAB(r?)0/a	CSRG	12.67	3201 ± 26	42.7 ± 3.0
NGC 7098	(R)SAB(r)a	CSRG	11.63	2381 ± 6	30.9 ± 2.2
NGC 7187	(R)SAB(r)0 ⁺	CSRG	13.42	2670 ± 21	37.0 ± 2.6
NGC 7219	(R' ₂)SA(r)b	CSRG	13.07	2956 ± 10	39.2 ± 2.7
NGC 7267	(R' ₁)SB(rs)a	CSRG	12.80	3355 ± 12	46.3 ± 3.2
NGC 7329	SB(r)b	CSRG	12.03	3252 ± 4	43.1 ± 3.0
NGC 7417	(R')SB(r)a	CSRG	12.93	3196 ± 22	42.1 ± 3.0
NGC 7531	SAB(r)bc	CSRG	11.41	1596 ± 3	21.5 ± 1.5
NGC 7702	(R)SAB(r)0 ⁺	CSRG	13.03	3231 ± 24	43.2 ± 3.0
IC 1438	(R ₁ R' ₂)SAB(s)ab	CSRG	12.46	2596 ± 3	36.6 ± 2.6
IC 4754	(R')SB(r)ab	CSRG	13.79	4406 ± 50	59.1 ± 4.2
IC 5240	SB(r)ab	CSRG	12.29	1765 ± 7	23.9 ± 1.7
UGC 12646	(R' ₁)SB(r)b	deVA	13.67	8034 ± 7	112.6 ± 7.9
ESO 152–26	(R ₁ R' ₂)SAB(r)ab	CSRG	13.95	6157 ± 27	82.7 ± 5.8

^aColumn 1: galaxy name; Column 2: galaxy classification; Column 3: source of the galaxy classification where deVA is from the de Vaucouleurs Atlas of Galaxies (Buta et al. 2007) and CSRG is from the Catalogue of Southern Ringed Galaxies (Buta 1995); Column 4: the corrected total apparent magnitude of the galaxy; Column 5: heliocentric velocity of the galaxy; Column 6: the galactocentric distance from NED.

^bAll ring parameters are for inner rings except for NGC 7020 whose measured values are for the outer ring.

Table 3. Planetary Nebulae H α Emission^a

Name	Aperture (")	This Paper (GB) (erg s ⁻¹ cm ⁻²)	Kohoutek (KM) (erg s ⁻¹ cm ⁻²)	$\log(\frac{F_{GB}}{F_{KM}})$
NGC 6326	34.8	3.96×10^{-11}	3.43×10^{-11}	0.06
NGC 6326	34.8	3.84×10^{-11}	3.43×10^{-11}	0.05
NGC 6818	43.4	1.43×10^{-10}	1.30×10^{-10}	0.04
NGC 6818	43.4	1.50×10^{-10}	1.30×10^{-10}	0.06

^aColumn 1: name of planetary nebula; Column 2: size of the aperture used to measure H α + [NII] flux emitted from the nebula; Column 3: H α + [NII] flux measured for this paper by Grouchy et al.(GB); Column 4: H α + [NII] flux measured by Kohoutek & Martin (KM); Column 5: The log of the ratio of the fluxes measured by Grouchy et al. (GB) to that measured by Kohoutek & Martin (KM).

Table 4. Galaxy H α emission^a

Name	ID	Radius (")	$F_{H\alpha+[NII]}$ ($\frac{10^{-14} \text{ ergs}}{s \text{ cm}^2}$)	% Error Cont Sub	$\log L_{H\alpha+[NII]}$	$L_{H\alpha}^0$ ($10^{41} \text{ ergs s}^{-1}$)	SFR ($M_{\odot} \text{ yr}^{-1}$)	W_{λ}
ESO 111-22	s	65.16	21.5 ± 7.4	2.8	41.66 ± 0.37	8.6 ± 3.2	6.8 ± 2.5	25.9 ± 4.4
ESO 198-13	l	43.44	23.0 ± 7.9	0.1	41.17 ± 0.37	2.8 ± 1.1	2.3 ± 0.8	16.8 ± 4.7
ESO 231-1	p	34.75	59.9 ± 20.7	2.0	41.88 ± 0.37	16.4 ± 6.1	13.1 ± 4.9	28.9 ± 5.0
ESO 234-11	m	47.78	3.3 ± 1.1	4.3	40.36 ± 0.37	0.5 ± 0.2	0.4 ± 0.1	2.4 ± 4.6
ESO 236-29	t	43.44	8.2 ± 2.8	5.5	41.71 ± 0.35	10.1 ± 3.6	8.0 ± 2.8	24.6 ± 4.6
ESO 286-10	k	86.88	19.0 ± 6.6	2.1	41.09 ± 0.37	2.5 ± 0.9	2.0 ± 0.7	4.3 ± 4.6
ESO 297-27	o	80.36	12.5 ± 4.3	7.1	41.04 ± 0.37	2.1 ± 0.8	1.7 ± 0.6	17.9 ± 4.8
ESO 399-25	g	43.44	8.9 ± 3.1	3.2	40.12 ± 0.37	0.3 ± 0.1	0.2 ± 0.1	1.0 ± 4.3
ESO 409-3	q	45.61	3.8 ± 1.3	8.6	40.80 ± 0.37	1.2 ± 0.5	1.0 ± 0.4	2.0 ± 4.7
ESO 526-7	n	106.43	25.0 ± 8.6	7.2	41.31 ± 0.37	5.0 ± 1.9	4.0 ± 1.5	7.9 ± 4.7
ESO 576-57	r	45.61	11.4 ± 3.9	9.1	40.72 ± 0.37	1.2 ± 0.4	0.9 ± 0.3	9.5 ± 4.7
IC 1993	c	65.59	9.0 ± 3.1	3.7	39.27 ± 0.37	0.04 ± 0.01	0.03 ± 0.01	1.6 ± 4.1
IC 5267	f	193.31	141.0 ± 48.8	4.5	40.96 ± 0.37	1.7 ± 0.7	1.4 ± 0.5	5.6 ± 3.8
NGC 5364	d	217	265.0 ± 91.5	5.1	40.95 ± 0.37	1.7 ± 0.7	1.4 ± 0.5	10.7 ± 4.0
NGC 5530	a	136.84	217.0 ± 75.1	0.7	40.74 ± 0.37	1.3 ± 0.5	1.0 ± 0.4	11.8 ± 4.0
NGC 7020	i	86.9	16.5 ± 5.7	0.4	40.56 ± 0.37	0.7 ± 0.3	0.6 ± 0.2	2.7 ± 4.2
NGC 7187	h	22.59	9.2 ± 3.2	2.5	40.18 ± 0.37	0.3 ± 0.1	0.2 ± 0.1	3.7 ± 3.8
NGC 7217	b	152	22.7 ± 7.8	1.1	39.84 ± 0.37	0.2 ± 0.1	0.1 ± 0.1	0.6 ± 4.3
NGC 7702	j	100	10.9 ± 3.8	3.7	40.39 ± 0.37	0.5 ± 0.2	0.4 ± 0.1	2.5 ± 4.2
NGC 7742	e	86.9	119.0 ± 41.2	2.4	40.94 ± 0.37	1.8 ± 0.7	1.5 ± 0.5	12.6 ± 4.4

^aColumn 1: galaxy name; Column 2: ID assigned to the galaxy which corresponds to the labels in Figure 1; Column 3: aperture radius used to measure the H α + [NII] flux emitted from each galaxy; Column 4: the H α + [NII] flux; Column 5: estimated error of the continuum subtraction calculated from the residuals of foreground stars; Column 6: the log of the H α + [NII] luminosity emitted from the galaxy; Column 7: the H α luminosity corrected for internal extinction, galactic extinction, and [NII] contamination; Column 8: the current SFR assuming a constant SFR through time, a solar metallicity, and a Salpeter (1955) IMF; Column 9: equivalent width of H α + [NII] emission.

Table 5. Calculated Sensitivity ($S(\lambda)$) of Our Filter System^{a,b}

	6477Å	6563Å	6606Å	6649Å	6693Å	6737Å	6781Å	6916Å
LTT 7987	11.62	10.05	10.57	10.82	11.75	10.07	10.06	11.42
LTT 7987	11.68	10.19	10.53	10.93	11.72	10.09	10.14	11.32
LTT 9239	11.65	9.98	10.50	10.88	11.78	10.08	10.14	11.41
LTT 9239	11.27	9.80	10.35	10.65	11.65	9.85	9.96	11.45
LTT 7987	n/a ^c	10.12	10.52	10.77	11.81	10.03	10.12	11.35
LTT 7987	n/a ^c	9.79	10.46	10.96	11.40	10.05	10.11	11.29
LTT 7987	n/a ^c	9.96	10.27	10.80	11.68	9.92	9.90	11.41
LTT 9239	n/a ^c	9.75	10.31	10.65	11.57	9.93	9.98	11.44
EG 274	n/a ^c	n/a ^d	10.36	10.78	11.72	10.10	n/a ^c	n/a ^c
$\langle S(\lambda) \rangle$	11.56	9.96	10.43	10.80	11.68	10.01	10.05	11.39
σ	0.19	0.16	0.11	0.11	0.13	0.09	0.09	0.06
$\langle \sigma \rangle$	0.10	0.06	0.04	0.04	0.04	0.03	0.03	0.02

^aRows 1 and 2: night four values of star LTT 7987; Rows 3 and 4: night four values of star LTT 9239; Rows 5 – 7: night five values for star LTT 7987; Row 8: night five value for star LTT 9239; Row 9: night five value for star EG 274; Row 10: the average value of $S(\lambda)$ for all stars; Row 11: the standard deviation of the mean; Row 12: the standard error of the mean.

^bAll values listed in units of 10^{-16} erg s⁻¹ cm⁻².

^cNo observation made.

^dImage not used due to tracking problems.

Table 6. Ring SFRs in the CBB96 Sample^{a,b}

Name	$\log F_{\text{H}\alpha+\text{[NII]}}$	r_{min} (")	Width (")	q	P.A. ($^{\circ}$)	Flux Fraction	SFR Ring	W_{λ} Ring
NGC 53	-12.99 ± 0.35	17.0	17.4	0.795	164.0	0.906	0.71 ± 0.21	11.9 ± 3.8
NGC 1317	-12.11 ± 0.33	39.1	26.1	1.000	90.0	0.045	0.05 ± 0.02	1.4 ± 0.5
NGC 1326	-11.62 ± 0.31	21.8	17.4	0.822	30.5	0.046	0.07 ± 0.02	3.1 ± 1.0
NGC 1350	-12.42 ± 0.34	53.9	37.0	0.499	13.0	0.630	0.29 ± 0.08	4.0 ± 1.3
NGC 1433	-11.57 ± 0.31	56.5	65.2	0.721	97.6	0.564	0.49 ± 0.14	13.6 ± 4.4
NGC 1832	-11.59 ± 0.31	13.1	10.9	0.768	147.7	0.191	0.70 ± 0.20	27.4 ± 8.8
NGC 6300	-11.50 ± 0.31	39.1	43.5	0.594	125.2	0.814	1.18 ± 0.34	24.1 ± 7.7
NGC 6753	-11.61 ± 0.31	8.7	4.3	0.840	57.1	0.124	1.26 ± 0.37	22.2 ± 7.1
NGC 6761	-12.89 ± 0.35	19.1	7.0	0.951	95.7	0.272	0.48 ± 0.14	10.2 ± 3.3
NGC 6782	-12.25 ± 0.33	17.4	15.7	0.643	175.6	0.240	0.84 ± 0.24	11.3 ± 3.6
NGC 6902	-11.95 ± 0.32	13.1	14.4	0.883	154.7	0.209	0.74 ± 0.22	12.6 ± 4.0
NGC 6935	-12.28 ± 0.33	11.4	17.4	0.860	0.8	0.647	2.73 ± 0.79	16.0 ± 5.1
NGC 6937	-12.05 ± 0.33	16.5	11.3	0.868	91.0	0.294	2.34 ± 0.68	46.4 ± 14.9
NGC 7020 ^b	-12.45 ± 0.34	52.6	52.2	0.484	162.0	0.448	0.62 ± 0.18	9.7 ± 3.1
NGC 7098	-12.18 ± 0.33	50.0	26.1	0.523	63.8	0.275	0.40 ± 0.12	13.5 ± 4.3
NGC 7187	-13.14 ± 0.36	13.9	8.7	0.968	123.3	0.557	0.12 ± 0.04	6.7 ± 2.1
NGC 7219	-12.56 ± 0.34	6.5	6.6	0.762	53.1	0.293	0.26 ± 0.08	12.3 ± 3.9
NGC 7267	-12.27 ± 0.33	25.2	8.7	0.601	99.0	0.121	0.28 ± 0.81	15.2 ± 4.9
NGC 7329	-12.16 ± 0.33	26.1	17.4	0.726	106.7	0.246	0.66 ± 0.19	14.0 ± 4.5
NGC 7417	-12.80 ± 0.35	17.4	13.1	0.701	28.2	0.203	0.12 ± 0.04	4.1 ± 1.3
NGC 7531	-11.90 ± 0.32	21.8	13.1	0.347	14.8	0.349	0.41 ± 0.12	24.7 ± 7.9
NGC 7702	-13.35 ± 0.36	28.3	8.7	0.463	113.7	0.000	0.00 ± 0.00	0.0 ± 0.0
IC 1438	-12.49 ± 0.34	14.4	14.4	0.641	124.0	0.300	0.28 ± 0.08	11.6 ± 3.7
IC 4754	-12.77 ± 0.35	15.2	7.8	0.869	47.2	0.393	0.58 ± 0.17	18.8 ± 6.0
IC 5240	-12.42 ± 0.34	33.9	10.4	0.632	106.8	0.262	0.11 ± 0.03	9.4 ± 3.0
UGC 12646	-12.53 ± 0.34	15.2	13.1	0.629	138.0	0.325	2.65 ± 0.77	32.2 ± 10.3
ESO 152–26	-12.75 ± 0.35	9.1	10.4	0.757	8.4	0.248	0.63 ± 0.18	12.0 ± 3.8

^aColumn 1: galaxy name; Column 2: log of total H α + [NII] flux based on improved continuum subtraction, to be compared with values in Column 2 of Table 2 of CBB96; Column 3: inner radius of elliptical annulus defining the inner ring (outer ring in the case of NGC 7020); Column 4: width of same elliptical annulus; Column 5: shape of elliptical annulus; Column 6: P.A. of elliptical annulus; Column 7: fraction of total H α flux included within this annulus; Column 8: ring SFR ($M_{\odot} \text{ yr}^{-1}$); Column 9: equivalent width of ring H α + [NII] (\AA), derived as in Romanishin (1990).

^bAll ring parameters are for inner rings except for NGC 7020 whose measured values are for the outer ring.

Table 7. Galaxy Ring Properties^a

Galaxy Name	Ring	a ($''$)	Width ($''$)	P.A. ($^\circ$)	q	SFR_{ring} ($M_\odot \text{ yr}^{-1}$)	$\frac{\text{SFR}_{ring}}{\text{SFR}_{total}}$
ESO 111–22	r	15.6 ± 0.1	5.0	8.8 ± 0.2	0.41 ± 0.03	1.2 ± 0.5	0.18
	R	48.9 ± 0.3	4.2	9.2 ± 0.1	0.45 ± 0.03	0.16 ± 0.06	0.02
ESO 198–13	nr	6.9 ± 0.1	1.4	-55.6 ± 0.6	0.75 ± 0.05	0.4 ± 0.1	0.17
	r	24.4 ± 0.3	2.0	64 ± 2	0.88 ± 0.05	1.1 ± 0.4	0.51
ESO 231–1	r	12.2 ± 0.1	4.6	66.4 ± 0.5	0.84 ± 0.05	5.8 ± 2.1	0.44
	R'	29.5 ± 0.2	4.2	-55.9 ± 0.7	0.83 ± 0.05	2.1 ± 0.7	0.16
ESO 234–11	r	10.8 ± 0.1	2.5	-62.5 ± 0.5	0.53 ± 0.03	0.09 ± 0.03	0.22
	R	31.7 ± 0.6	1.5	57.5 ± 0.3	0.40 ± 0.03	0.05 ± 0.02	0.13
ESO 236–29	nr	5.7 ± 0.1	2.3	73 ± 1	0.85 ± 0.05	0.6 ± 0.2	0.07
	r	19.3 ± 0.3	4.6	76 ± 2	0.62 ± 0.04	1.6 ± 0.5	0.19
ESO 286–10	R	60.5 ± 1.2	1.5	-46 ± 3	0.84 ± 0.03	0.08 ± 0.03	0.04
ESO 297–27	rs	18.0 ± 0.6	0.7	68 ± 2	0.65 ± 0.05	0.2 ± 0.1	0.10
ESO 399–25	R'	92.9 ± 2	0.4	-25.1 ± 0.3	0.31 ± 0.02	0.008 ± 0.003	0.04
ESO 409–3	R'	32.2 ± 0.2	3.2	-5 ± 1	0.88 ± 0.05	0.5 ± 0.2	0.53
ESO 526–7	r	27.0 ± 0.3	2.3	-74.3 ± 0.5	0.58 ± 0.04	0.6 ± 0.2	0.14
ESO 576–57	r	22.1 ± 0.4	1.4	14 ± 2	0.71 ± 0.05	0.12 ± 0.04	0.13
	R	34.4 ± 0.8	1.3	16 ± 3	0.81 ± 0.05	0.09 ± 0.03	0.10
IC 1993	R'	45.2 ± 0.3	0.7	57 ± 2	0.94 ± 0.02	0.03 ± 0.01	0.94
IC 5267	rs	78 ± 1	0.6	-50 ± 2	0.78 ± 0.02	0.07 ± 0.03	0.05
	R	147 ± 1	0.7	34.3 ± 0.2	0.68 ± 0.04	0.05 ± 0.02	0.04
NGC 5364	r	41.1 ± 0.6	1.4	44.5 ± 0.2	0.49 ± 0.03	0.13 ± 0.05	0.09
NGC 5530	rs	32.6 ± 0.7	1.0	-65.6 ± 0.7	0.54 ± 0.03	0.12 ± 0.04	0.12
NGC 7020	R	81.2 ± 0.7	2.7	-19.7 ± 0.2	0.49 ± 0.03	0.16 ± 0.06	0.27
NGC 7187	r	19.6 ± 0.2	1.6	84 ± 2	0.88 ± 0.05	0.13 ± 0.05	0.54
NGC 7217	r	11.1 ± 0.1	0.2	-86.4 ± 0.6	0.77 ± 0.05	0.01 ± 0.002	0.04
	R	76.7 ± 0.5	1.4	-86.1 ± 0.5	0.85 ± 0.05	0.2 ± 0.1	1.46
NGC 7702	r	32.6 ± 0.3	1.8	-61.7 ± 0.3	0.41 ± 0.03	0.07 ± 0.03	0.18
NGC 7742	r	9.4 ± 0.1	1.3	-50 ± 7	0.97 ± 0.06	1.3 ± 0.5	0.86

^aColumn 1: galaxy name; Column 2: ring feature; Column 3: average diameter of the H α ring feature; Column 4: width of aperture used to measure H α flux in the ring; Column 5: P.A. of elliptical aperture used. Zero is north with positive angles moving toward the east and negative to the west; Column 6: axis ratio of aperture; Column 7: SFR of ring; Column 8: fraction of the ring SFR to the galaxy’s total SFR.

Table 8. Non-axisymmetric Torque Strengths, Radial Scale Lengths and Deprojected Ring Parameters for 20 Nonbarred Ringed Galaxies^a

Name	r_{dep} (")	q_{dep}	h_r (")	Q_r	$A_2(ring)$	Q_g	r_{max} (")
ESO 111–22	15.7 ± 0.8	0.85 ± 0.04	22.6 ^b	0.041	0.191	0.073	48.2
ESO 198–13	7.1 ± 0.4	0.97 ± 0.05	10.5 ^b	0.018	0.048	0.070	29.1
ESO 231–1	12.7 ± 0.7	0.86 ± 0.05	9.4	0.072	0.057	0.104	17.8
ESO 234–11 ^c	32 ± 2	0.85 ± 0.04	23.8	0.017	0.146	0.042	13.5
ESO 236–29	8.5 ± 0.4	0.67 ± 0.04	12.0 ^b	0.037	0.148	0.090	16.9
ESO 286–10	67 ± 4	0.88 ± 0.05	38.2	0.031	0.266	0.059	17.8
ESO 297–27	25 ± 1	0.59 ± 0.05	11.8	0.049	0.124	0.082	4.8
ESO 399–25 ^c	93 ± 5	0.67 ± 0.04	41.0 ^b	0.041	0.325	0.061	11.7
ESO 409–3	34 ± 2	0.90 ± 0.05	9.7 ^b	0.068	0.359	0.068	32.6
ESO 526–7	30 ± 2	0.75 ± 0.04	24.7 ^b	0.049	0.170	0.051	25.6
ESO 576–57	22 ± 1	0.85 ± 0.05	18.4	0.018	0.069	0.040	41.3
IC 1993	46 ± 2	0.95 ± 0.05	27.7 ^b	0.029	0.072	0.043	30.8
IC 5267	80 ± 4	0.92 ± 0.05	28.4 ^b	0.039	0.166	0.076	28.7
NGC 5364	42 ± 2	0.59 ± 0.03	59.5	0.093	0.210	0.106	36.1
NGC 5530 ^c	41 ± 2	0.73 ± 0.04	41.0	0.061	0.077	0.123	10.0
NGC 7020	90 ± 5	0.89 ± 0.05	26.3 ^b	0.021	0.050	0.074	34.3
NGC 7187	21 ± 1	0.82 ± 0.05	16.6 ^b	0.077	0.338	0.077	21.3
NGC 7217	11.5 ± 0.6	0.85 ± 0.04	56.0 ^b	0.029	0.061	0.045	38.9
NGC 7702 ^c	33 ± 2	0.80 ± 0.04	54.0	0.081	0.395	0.084	30.8
NGC 7742	9.8 ± 0.5	0.96 ± 0.05	13.1	0.058	0.101	0.058	9.1

^aColumn 1: galaxy name; Columns 2 and 3: deprojected radius and axis ratio of the main ring, typically the inner ring, as seen in the H α image. Values are based on an ellipse fit to the H α distribution in the ring. If the ring was not visible in the H α then the parameters are based on the *B*-band image and the galaxy name is marked with the letter “c”; Column 4: radial scale length based on one-dimensional (denoted with the letter “b”) and two-dimensional decompositions (see the text and Grouchy (2008)); Column 5: gravitational torque strength at the location of the ring’s major axis; Column 6: the $m = 2$ Fourier amplitude at the position of the ring’s major axis; Column 7: maximum relative non-axisymmetric torque strength based on Grouchy (2008) *I*-band images; Column 8: the radius of the Q_g .

^bOne-dimensional fits to the disk of the surface brightness profile were used for these galaxies in which the two-dimensional decomposition had difficulty fitting the disk.

^cThese rings had no detectable H α emission; therefore, the ring parameters were taken from the broadband stellar ring.

Table 9. Bar Strengths, Radial Scale Lengths and Deprojected Ring Parameters for the CBB96 Sample^a

Name	r_{dep} (")	q_{dep}	h_r (")	Q_r	$A_2(ring)$	Q_g	r_{max} (")
NGC 53	30 ± 2	0.88 ± 0.04	30.6	0.244	0.438	0.353	20.4
NGC 1317	61 ± 3	0.82 ± 0.04	19.1	0.016	0.087	0.111	4.8
NGC 1326	42 ± 2	0.71 ± 0.04	34.9	0.178	0.634	0.180	37.4
NGC 1350	81 ± 4	0.77 ± 0.04	68.1	0.211	0.663	0.237	68.1
NGC 1433	105 ± 5	0.62 ± 0.03	62.9	0.326	0.912	0.400	67.0
NGC 1832	25 ± 1	0.69 ± 0.03	16.1	0.056	0.261	0.176	44.7
NGC 6300	69 ± 4	0.71 ± 0.04	37.3	0.191	0.425	0.220	32.2
NGC 6753	11.5 ± 0.6	0.88 ± 0.04	21.4	0.043	0.109	0.053	36.9
NGC 6761	23 ± 1	0.96 ± 0.05	15.8	0.182	0.210	0.347	15.2
NGC 6782	26 ± 1	0.65 ± 0.03	28.5	0.167	0.666	0.172	23.9
NGC 6902	25 ± 1	0.85 ± 0.04	34.5	0.084	0.238	0.086	28.7
NGC 6935	22 ± 1	0.90 ± 0.05	22.6	0.058	0.129	0.064	23.0
NGC 6937	28 ± 1	0.70 ± 0.04	34.7	0.182	0.419	0.282	20.4
NGC 7020	87 ± 4	0.90 ± 0.05	40.5	0.086	0.354	0.086	34.3
NGC 7098	66 ± 3	0.83 ± 0.04	49.7	0.126	0.418	0.159	46.1
NGC 7187	20 ± 1	0.92 ± 0.05	30.7	0.065	0.299	0.067	20.4
NGC 7219	12.3 ± 0.6	0.72 ± 0.04	14.8	0.141	0.496	0.142	11.7
NGC 7267	33 ± 2	0.54 ± 0.03	14.8	0.242	0.517	0.549	15.2
NGC 7329	39 ± 2	0.93 ± 0.05	34.1	0.164	0.306	0.279	28.2
NGC 7417	29 ± 2	0.70 ± 0.04	21.7	0.149	0.300	0.232	18.7
NGC 7531	29 ± 2	0.72 ± 0.04	24.3	0.154	0.387	0.154	27.0
NGC 7702	33 ± 2	0.77 ± 0.04	34.2	0.140	0.654	0.142	30.8
IC 1438	23 ± 1	0.66 ± 0.03	23.4	0.152	0.681	0.159	20.4
IC 4754	22 ± 1	0.79 ± 0.04	15.1	0.127	0.181	0.324	11.7
IC 5240	40 ± 2	0.87 ± 0.04	24.8	0.145	0.332	0.273	26.5
UGC 12646	24 ± 1	0.57 ± 0.03	32.0	0.306	1.090	0.318	22.1
ESO 152-26	17.4 ± 0.9	0.81 ± 0.04	24.5	0.143	0.486	0.165	13.5

^aColumn 1: galaxy name; Columns 2 and 3: deprojected radius and axis ratio of the main ring, typically the inner ring, as seen in the H α image. These values are based on an ellipse fit to the H α distribution in the ring; Column 4: radial scale length based on two-dimensional decompositions (see the text and Grouchy(2008)); Column 5: gravitational torque strength at the location of the ring’s major axis; Column 6: the $m = 2$ Fourier amplitude at the position of the ring’s major axis; Column 7: maximum relative non-axisymmetric torque strength based on Grouchy (2008) I -band images; (8) the radius of the Q_g .